Astronomy & Astrophysics manuscript no. output
July 13, 2026

Shape, orientation, and colors-combined approach for asteroids (SOCCA)

K. O. Xenos[1,2], B. Carry[1], J. Peloton[3], M. Mahlke[4,5], J. Berthier[6], and P.-A. Mattei[7]

[1] Université Côte d'Azur, Observatoire de la Côte d'Azur, CNRS, Laboratoire Lagrange, France
[2] MAUCA - Master track in Astrophysics, Université Côte d'Azur & Observatoire de la Côte d'Azur, Parc Valrose, 06100, Nice, France
[3] Université Paris-Saclay, CNRS/IN2P3, IJCLab, 91405 Orsay, France
[4] Institut d'Astrophysique Spatiale, Université Paris-Saclay, CNRS, F-91405 Orsay, France
[5] Université Marie et Louis Pasteur, CNRS, Institut UTINAM (UMR 6213), équipe Astro, 25000 Besançon, France
[6] IMCCE, Observatoire de Paris, PSL Research University, CNRS, Sorbonne Universités, UPMC Univ Paris 06, Univ. Lille, 75014 Paris, France
[7] Université Côte d'Azur, Inria, Maasai project-team, Laboratoire J.A. Dieudonné, UMR CNRS 7351, France

Received April 03, 2026; accepted June 16, 2026

ABSTRACT

Context. Large photometric surveys provide sparse multiband photometry for millions of Solar System objects (SSOs), offering an opportunity to jointly constrain their physical and compositional properties. However, current phase-function models do not account for rotational variability, limiting their ability to retrieve accurate parameters. Similarly, methods that recover shape and rotational parameters remain both computationally and observationally expensive, making the extraction of such properties prohibitive at scale.

Aims. We aim to develop a model capable of simultaneously retrieving the absolute magnitude, phase parameters, spin state, and shape proportions of SSOs from sparse photometric data, while remaining computationally efficient for large datasets.

Methods. We introduce the Shape, orientation, and colors-combined approach for asteroids (SOCCA), which extends the HG_1G_2 formalism by incorporating the projected surface of a rotating triaxial ellipsoid. The model jointly fits multiband photometry and includes a dedicated treatment of rotational period determination.

Results. We implemented the model on a ten-year Legacy Survey of Space and Time (LSST) simulation as well as on real data of the asteroid (45) Eugenia for validation purposes. SOCCA significantly improves the fit to photometric data, reducing the mean residuals to half, compared to previous models. It retrieves the absolute magnitude with a scatter about three times smaller than existing approaches and improves the determination of phase parameters by a similar factor. It also recovers the sidereal rotation period, spin-axis orientation, and the axis ratios of the best fitting ellipsoid. The inclusion of shape and rotation increases the number of physically meaningful solutions by ∼10-20% per filter, leading to an overall success rate of 53%.

Conclusions. By combining phase, shape, and rotational information in a single model, SOCCA provides a more complete physical description of SSOs from sparse photometry. Its performance and scalability make it well suited for current and upcoming large surveys such as the *Zwicky* Transient Facility and the recently launched LSST.

Key words. methods: data analysis – methods: numerical – techniques: photometric – minor planets, asteroids: general

1. Introduction

The asteroids and comets, hereafter referred to as Solar System objects (SSOs), are the remnants of the planetesimals, the building blocks that accreted to form the planets 4.6 Gy ago (Johansen et al. 2015; Morbidelli et al. 2022). Their composition, studied via remote sensing observations and laboratory analysis of meteorites, inform us of the place and timing of their formation in the protoplanetary disk around the young Sun (Scott et al. 2018; Neveu & Vernazza 2019). The subsequent stages of planetary formation such as planet migration and dynamical instability (e.g., Walsh et al. 2011; Clement et al. 2020) defined how these compositions are distributed in the Solar System (DeMeo & Carry 2014).

Their current distribution is, however, a degraded version of this original, post-planetary formation distribution. First, gigayears of collisions have created localized overrepresentation of compositions (the dynamical families; Hirayama 1918; Novaković et al. 2022). Second, the secular dynamical evolution described by the Yarkovsky effect (Vokrouhlický et al. 2015) has slowly diffused structures (Bottke et al. 2001). This process of collisional grinding and orbital drift is responsible for the injection of objects in near-Earth space: the near-Earth objects and, ultimately, the meteorites (Farinella et al. 1998), which are our compositional references (DeMeo et al. 2022).

A deep understanding of the original distribution of planetesimals hence requires a large corpus of SSOs with both dynamical and compositional information, together with their long-term evolution. The present study focused

Article published by EDP Sciences, to be cited as https://doi.org/10.1051/0004-6361/202660190

on the development of a method to jointly determine the colors and physical properties of SSOs in order to provide observational constraints on both aspects.

Multiple colors defined as the difference of magnitude in two photometric filters, over the visible and near-infrared wavelength ranges can be used to taxonomically classify SSOs (Gradie & Tedesco 1982; DeMeo & Carry 2013; Popescu et al. 2018). Each class is based on spectral features (Tholen 1984; Mahlke et al. 2022) and can be used as proxy for composition thanks to dedicated analyses of individual SSOs and comparison with meteorites, returned samples, and minerals in the lab (McCord et al. 1970; Brownlee et al. 2006; Nakamura et al. 2011; Cloutis et al. 2015; Nakamura et al. 2023; Lauretta et al. 2024; Mahlke et al. 2026).

The long-term evolution, due to semimajor drift by the nongravitational Yarkovsky effect, is directly affected by the physical parameters of the SSO: diameter, albedo, obliquity, rotation period, density, and thermal inertia (Vokrouhlický et al. 2015). It has been shown that Yarkovsky and the associated torque YORP (ibid), which changes the spin, are not constant over long timescales but have a stochastic evolution owing to small changes on the surface of these objects (craters and landslides; see Statler 2009; Bottke et al. 2015; Zhou & Michel 2024). We lack a large sample of SSOs with measured physical parameters to fully assert the timescale and amplitude of this stochastic evolution, despite recent progress (Zhou et al. 2025).

The sample of SSOs with taxonomic classification has been limited to small number statistics for decades. Most determinations were obtained by targeted surveys, aimed at obtaining the spectral reflectance or the colors of the objects (McCord et al. 1970; McCheyne et al. 1985; Birlan et al. 1996; Moskovitz et al. 2008). This corpus has dramatically increased over the last decade, mainly thanks to large sky surveys that provided near-simultaneous multi-filter observations (such as the SDSS, SkyMapper, and VISTA; see Wolf et al. 2018; McMahon et al. 2013; Carvano et al. 2010; DeMeo & Carry 2013; Popescu et al. 2018; Sergeyev & Carry 2021; Sergeyev et al. 2022) or spectra (Gaia; Prusti et al. 2016; Galluccio et al. 2023; Tanga et al. 2023). The current sample[1] of visible spectra contains over 60,000 asteroids; visible colors are available for 429,000, and near-infrared colors for about 35,000 of them.

The determination of physical parameters has followed a parallel evolution. From the first historical diameter and albedo determinations (e.g., Morrison 1974; Wasserman et al. 1979), IRAS (Neugebauer et al. 1984) was the first survey to provide 2000 asteroids (Sykes et al. 2000), and the all-sky mid-infrared space missions WISE (Wright et al. 2010) and AKARI (Murakami et al. 2007) brought the sample to 149,000 (Usui et al. 2011; Hasegawa et al. 2013; Mainzer et al. 2011; Grav et al. 2011; Masiero et al. 2011; Bauer et al. 2012). Rotation periods were traditionally studied by acquiring time-dense time-series photometry (generally referred to as light curves; see Russell 1906; Schober & Dvorak 1975; French 1987; Pilcher 2012); this was a highly telescope-time-consuming process. Data mining of wide-field photometry surveys built for the transient sky (such as the PTF; Law et al. 2009) or exoplanet detection by the transit method (e.g., *Kepler*/K2 and TESS; Borucki et al. 2010; Howell et al. 2014; Ricker et al. 2015) have recently produced many rotation periods (Waszczak et al. 2015; Chang et al. 2015; Pál et al. 2020; Kecskeméthy et al. 2023; Vavilov & Carry 2025). Yet, the total number remains limited to 51,000, which is much smaller that the known population of 1.5 million SSOs.

The remaining properties are the least constrained: spin orientation (spin coordinate and obliquity; about 60,000 SSOs), density (500), and thermal inertia (2,000). Density requires a mass estimate, which is arguably the most difficult property to measure for SSOs (Carry 2012; Scheeres et al. 2015). The large collection of mid-infrared data from IRAS, AKARI, and WISE, and the upcoming NASA NEO Surveyor and ESA NEOMIR missions (Mainzer et al. 2023; Conversi et al. 2024), could lead to the determination of thermal inertia for numerous SSOs through thermophysical modeling (Lagerros 1996; Jiang & Ji 2021). The limiting factor is, however, the availability of the spin properties (and shape).

Light curves obtained under different Sun–target–observer geometries (i.e., generally obtained over multiple years) have been used for 50 years to determine the spin and simple triaxial-ellipsoid shape of asteroids (e.g., Surdej & Surdej 1977; Ostro & Connelly 1984). A major improvement occurred at the turn of the twentieth century with what is now called the standard light-curve inversion (LCI; Kaasalainen & Torppa 2001; Kaasalainen et al. 2001), providing a robust method for spin and convex-shape determination (other successful approaches are also in use, such as Bartczak & Dudziński 2018; Cellino et al. 2019; Muinonen et al. 2020). The LCI approach is also applicable to sparse photometry (that is photometry acquired with a time sampling typically larger than the rotation period of the target; Kaasalainen 2004) partly overcoming the limitation imposed by the telescope-time-consuming aspect of light curves. In twenty years, the application of the LCI to Lowell, WISE, Atlas, Gaia photometry brought the number of spin and shape determinations to almost 11,000 asteroids (e.g., Ďurech et al. 2016, 2018, 2020). Nevertheless, the fraction of successful fits compared to the sample of SSOs (hereafter the success rate) remains limited and time consuming to obtain. (see Ďurech et al. 2015; Cellino et al. 2024; Ďurech & Hanuš 2023)

The benefit of using large-sky surveys for studying the composition and physical properties of SSOs is clear, owing to the amount of observations they produce. This is particularly true for the Legacy Survey of Space and Time (LSST) of the *Vera C. Rubin* Observatory (Ivezić et al. 2019), which is expected to return around 400 observations in six filters (u, g, r, i, z, y; Roodman et al. 2024) for about five million SSOs (Kurlander et al. 2025). The challenge remains in identifying SSOs in these surveys (source of potential outliers from mis-associations) and handling data not solely optimized for SSO science. This mostly applies to cadence, i.e., the time interval between frames; the SSOs are thus selected based on their apparent motion and may preclude the direct computation of colors if the acquisition of different filters is too separated in time (see the discussions in Popescu et al. 2016; Carry 2018).

We built upon the recent $\texttt{sHG}_1\texttt{G}_2$ model (Carry et al. 2024) to combine two approaches—phase function and

[1] All numbers are extracted from the `SsODNet` service (Berthier et al. 2023), which is arguably the largest collection of properties of SSOs: https://ssp.imcce.fr/webservices/ssodnet/
The spectra themselves can be accessed through `classy`: https://github.com/maxmahlke/classy

spin/shape modeling—in a general approach: Shape, orientation, and colors-combined approach for asteroids (SOCCA). It provides the absolute magnitudes in multiple filters, and hence the colors, together with the spin and shape of SSOs, from sparse, multi-filter photometry such as that provided by large sky surveys.

We present the SOCCA model in Sect. 2 and the determination of its initial parameters, crucial for a successful fit, in Sect. 3. We go into more detail concerning the initialization of the rotational period in Sect. 4 and then validate our approach in Sect. 5 based on simulated observations of SSOs on real data. In Sect. 6 we present an evaluation of the algorithm's performance on real data of the asteroid (45) Eugenia. Finally in Sect. 7 we discuss certain improvements and extensions to the model, and in Sect. 8 we summarize the work presented and lay out some conclusions.

2. The SOCCA model

The apparent magnitude m of an SSO in any filter can be expressed as its intrinsic absolute magnitude H (in the same filter) modulated by the changing geometry of observations:

$$m = H + f(r, \Delta) + g(\gamma) + s(\alpha, \delta, t), \tag{1}$$

,
where the function $f(r, \Delta)$ accounts for the changing Sun–target and target–observer distances; the function $g(\gamma)$ describes the evolution of brightness with the phase angle (γ, the Sun–target–observer angle); and the function $s(\alpha, \delta, t)$ is the ever-changing apparent shape of the target.

Broadly, Eq. 1 is referred to as the phase function. The first version was written by Bowell et al. (1989). Since 2012, the IAU recommendation is to use the following formalism by Muinonen et al. (2010):

$$\begin{aligned} f(r, \Delta) &= 5 \log_{10}(r\Delta) & (2)\\ g(\gamma) &= -2.5 \log_{10} [\mathtt{G}_1 \phi_1(\gamma) \\ &\quad + \mathtt{G}_2 \phi_2(\gamma) \\ &\quad + (1 - \mathtt{G}_1 - \mathtt{G}_2)\phi_3(\gamma)] & (3) \end{aligned}$$

.
We adopted the updated constraints on $\mathtt{G}_1$ and $\mathtt{G}_2$ proposed by Oszkiewicz et al. (2026):

$$\mathtt{G}_1 \geq -0.429 \tag{4a}$$
$$\mathtt{G}_2 \leq 1.429 \tag{4b}$$
$$\mathtt{G}_2 \geq -0.4\,\mathtt{G}_1 \tag{4c}$$
$$\mathtt{G}_2 \geq -3.9038\,\mathtt{G}_1 - 0.2445 \tag{4d}$$
$$\mathtt{G}_2 \leq -0.9635\,\mathtt{G}_1 + 1.0157 \tag{4e}$$

The $s(\alpha, \delta, t)$ function was only recently introduced by Carry et al. (2024) to solve a common phase-function issue: the variation of absolute magnitude from apparition to apparition (e.g., Mahlke et al. 2021; Colazo et al. 2025). This variation is due to the slowly changing geometry (i.e., the angle between the target spin axis and the viewing direction, called the aspect angle, Λ) under which the shape of the SSO is seen (Jackson et al. 2022). Splitting observations by apparitions only provides a partial solution: the aspect angle evolves within an apparition, and the $\mathtt{G}_1\mathtt{G}_2$ parameters are thus biased as the $g(\gamma)$ function attempts to fit a signal that is a combination of phase- and shape-related variability (see Fig. 2 in Carry et al. 2024).

The introduction of this shape-related component to the phase function practically solves the apparition-to-apparition effect: it increases the success rate of the model fit, it improves residuals between observations and model, and the $\mathtt{G}_1\mathtt{G}_2$ parameters are more clustered per taxonomic class (see Carry et al. 2024). The recently introduced $s(\alpha, \delta, t)$ function described the geometry of a simple oblate spheroid (of diameters $a = b \geq c$), i.e., it was explicitly independent of time (i.e., $s(\alpha, \delta, t) = s(\alpha, \delta)$; see Appendix A). However, not all SSOs are simple spheroids, and many are elongated (Thirouin et al. 2018). This leads to a non-modeled, high-frequency component in the residuals, linked with the rotation of the targets. Furthermore, the derived spin coordinates (α_0, δ_0) are ambiguous (as intuited by Russell 1906), with a mirror solution at (α_0 +180°, $-\delta_0$) fitting the observations equally well.

We thus generalized the shape function $s(\alpha, \delta, t)$ to account for the rotation of a triaxial ellipsoid. The proposed SOCCA approach is conceptually close to the ellipsoid fit by Cellino et al. (2019, 2024), but it uses the IAU-approved phase function $g(\gamma)$ instead of the more restrictive linear slope. This model is also resemblant of the LCI approach (in which the phase function is described by a linear-exponential function; Kaasalainen et al. 2001), but it strives to 1) fit the apparent magnitudes (LCI handles relative fluxes) to derive the colors of the target from the absolute magnitudes obtained in different filters, and 2) to maintain a limited number of free parameters (ellipsoid case, which also provides a significantly faster computation; Ďurech et al. 2016).

We modeled the shape of an SSO with an ellipsoid of semi-axes, $a > b > c$, in a target-centric reference frame where the axes (x, y, z) are aligned with the longest, middle, and shortest axes. The ellipsoid rotates with a sidereal period $\mathtt{P}_{\rm sid}$ along the z-axis, whose coordinates are (α_0, δ_0) in the equatorial reference frame (taken at J2000 epoch, i.e., EQJ2000). Following Ostro & Connelly (1984), we computed the brightness of the ellipsoid as its projected area on the plane of the sky, accounting for both the limb and the terminator (the complete description is provided in Appendix A). The definition of the absolute magnitude H must therefore be updated; this is the magnitude of the object at 1 au from both the Sun and the observer, with a 0° phase angle, seen from its equatorial plane and its prime meridian.

In Fig. 1 we compare the $s(\alpha, \delta)$ (Carry et al. 2024) and the proposed $s(\alpha, \delta, t)$ functions defining the $\mathtt{sHG}_1\mathtt{G}_2$ and SOCCA models. The difference is most notable against the rotation phase; the $\mathtt{sHG}_1\mathtt{G}_2$ model is invariant, while SOCCA presents a double-peaked light curve built in $s(\alpha, \delta, t)$ as a rotating ellipsoid. The two models also differ against the aspect angle. The $s(\alpha, \delta, t)$ is smoother than the ad hoc function of $\mathtt{sHG}_1\mathtt{G}_2$ and presents a larger amplitude than $s(\alpha, \delta)$.

In summary, SOCCA captures both the short- and the long-term photometry of SSOs with a frugal approach, i.e., with a minimalistic number of free parameters:

- Three (H, $\mathtt{G}_1$, $\mathtt{G}_2$) for the behavior compared to the phase angle
- Two (α_0, δ_0) for the orientation of the spin axis

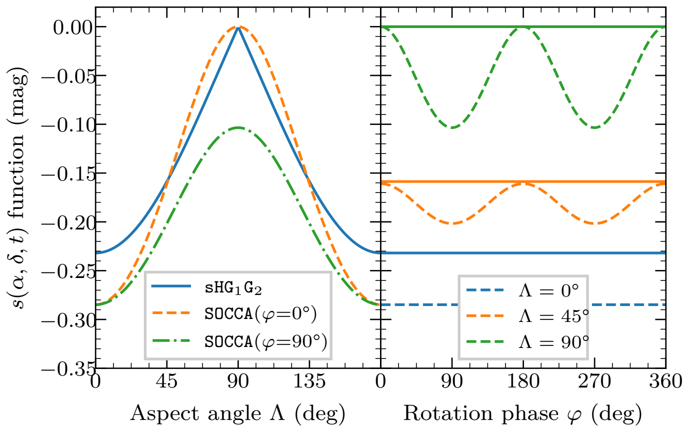

Fig. 1: Comparison of the behavior of shape function $s(\alpha, \delta, t)$ of `sHG1G2` (solid lines) and `SOCCA` (dashed lines) compared to aspect angle (Λ; *left*) and rotation phase (φ; *right*).

– Two ($\mathtt{P}_{\mathrm{sid}}$, W_0) for the rotation around the spin axis
– Two (a/b, a/c) representing the shape of the ellipsoid

Among these, the latter six parameters describing the geometry are wavelength independent. The former three parameters can, however, be different for each observed filter: the colors of SSOs result from different H in different filters, and it has been shown that $\mathtt{G}_1\mathtt{G}_2$ are wavelength dependent (and responsible for the so-called phase reddening; e.g., Sanchez et al. 2012; Mahlke et al. 2021). Hence, the total number of free parameters is $3N_F$ +6 for observations acquired in N_F different filters. It represents five more than $\mathtt{HG}_1\mathtt{G}_2$ (Muinonen et al. 2010), but only three more than $\mathtt{sHG}_1\mathtt{G}_2$ (Carry et al. 2024) to account for the full geometry. Even with the six filters of LSST (i.e., $N_F = 6$), the model is over-constrained (i.e., there are many more data points than free parameters) for large numbers of observations, and the parameters can be determined by χ^2 minimization as long as there is adequate phase and aspect (i.e., line-of-sight–spin axis) angle coverage in the photometric data. That is required in order to constrain the $\mathtt{G}_1$-$\mathtt{G}_2$ and a/b-a/c parameters, respectively.

3. Initializing the model

While `SOCCA` strives to minimize the number of free parameters, the parameter space still represents a large volume to explore and contains many local minima. The convergence of the phase-related function $g(\gamma)$ is expected to be smooth (Fig. 2), provided observations at low phase angles are secured (below ≈5°; see Mahlke et al. 2021, for a discussion on the need for near-opposition observations). The shape-related function $s(\alpha, \delta, t)$ is more likely to present numerous local minima for the spin coordinates (α_0, δ_0), and even more so for the sidereal rotation period $\mathtt{P}_{\mathrm{sid}}$ (a well-documented aspect of shape inversion; see Ďurech et al. 2015, for a review).

We tackled this issue with the objective of remaining frugal. The number of SSOs strongly increases with LSST (Kurlander et al. 2025), and the number of observations increases even more (LSST Science Collaboration et al. 2009). To fit all these observations while minimizing the needed resources and their impact, we focused on limiting computations rather than expensive grid searches. We thus used a combination of a $\mathtt{sHG}_1\mathtt{G}_2$ fit and a frequency analysis to estimate the optimum initial conditions to determine the parameters of `SOCCA` through traditional gradient-descent least-squares minimization. In this section we describe the initialization of most parameters and discuss the more complex rotation period next.

3.1. Phase and shape

While the definition of H differs between $\mathtt{sHG}_1\mathtt{G}_2$ and `SOCCA`, it only acts as a small global photometric offset, which is easily captured by the model (Fig. 2). The phase-function $g(\gamma)$ parameters, $\mathtt{G}_1\mathtt{G}_2$, are strictly similar on the other hand. We thus directly initiated `SOCCA` inversion with the H, $\mathtt{G}_1$, and $\mathtt{G}_2$ obtained from $\mathtt{sHG}_1\mathtt{G}_2$ modeling.

The description of the shape between the two models improved from oblate spheroid to triaxial ellipsoid. The residuals of the $\mathtt{sHG}_1\mathtt{G}_2$ modeling are thus due to the non-modeled short-term variability, which is linked with a/b and can in turn be estimated from the peak-to-peak amplitude, A, of the residuals. This, together with the relation between the oblateness, R, and the axis ratios (Eq. A.2; Carry et al. 2024), gives

$$\mathtt{a/b} = 10^{0.4A} \quad (5)$$
$$\mathtt{a/c} = (\mathtt{a/b} + 1)/2R\,. \quad (6)$$

.

3.2. Spin-axis orientation

The $\mathtt{sHG}_1\mathtt{G}_2$ fit provides a spin solution (α_0, δ_0) and its mirror solution (α_0 +180°, -δ_0). Rather than initializing `SOCCA` at these two coordinates only, we performed an additional safety check. We computed the root mean square (RMS) of $\mathtt{sHG}_1\mathtt{G}_2$ residuals on a grid of spin-axis coordinates spanning the entire celestial sphere: $\alpha_0 \in [0°, 360°[$ and $\delta_0 \in [-90°, 90°]$, with steps of 10° and 5°, respectively. We only did forward computation of $\mathtt{sHG}_1\mathtt{G}_2$, keeping all parameters but the spin coordinates fixed. It is therefore a computationally light and fast grid.

We smoothed the resulting RMS map with a Gaussian kernel density estimate of width 4° to suppress high-frequency noise. This scale is comparable to the typical uncertainty on (α, δ), and the exact choice has little impact on the result. Local minima were then identified on the interpolated map by running a 7.5° × 3.75° two-dimensional window minimum filter. The resulting (α_0, δ_0) solutions were each tested as initial points for the `SOCCA` fit.

4. Rotational period

4.1. Finding the synodic period

Photometric data from sky surveys typically span many years: 8 y for the *Zwicky* Transient Facility (ZTF; Bellm et al. 2019); 9 y for ATLAS (Tonry et al. 2018)—we used this later to illustrate `SOCCA` on real data (Sect. 6)—and 10 y for the LSST (Ivezić et al. 2019). The rotation periods of SSOs are much shorter—from about 2 h to a few days—half of known periods are shorter than 12 h (Berthier et al. 2023), but there is a bias against observing slow rotators;

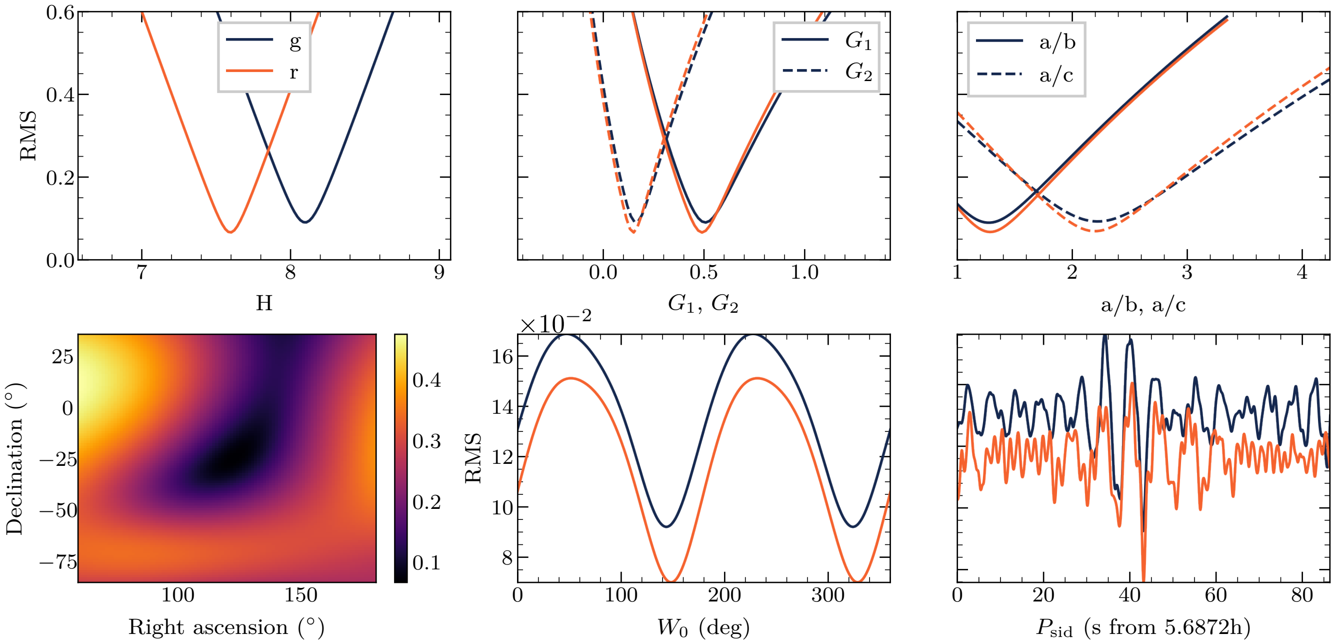

Fig. 2: Dependence of SOCCA on its parameters illustrated with (45) Eugenia. All but the sidereal periods have a smooth convergence to the best-fitting values.

see Marciniak et al. (2018). Hence, any deviation from the true sidereal period, $\mathtt{P}_{\rm sid}$, in the initialization of the SOCCA fit would lead to a significant de-phasing of the viewing geometry (the sub-observer longitude, φ; Appendix A) over the observation epochs. Owing to the forest of local minima in the sidereal period ($\mathtt{P}_{\rm sid}$) space (Fig. 2), a robust method for its initialization is required.

As stated in Sect. 3.1, the residuals of $\mathtt{sHG_1G_2}$ are due to the non-modeled rotation. We thus searched for periodicity in these residuals using Lomb–Scargle frequency analysis (Lomb 1976; Scargle 1982). It is nontrivial, and caution must be applied. First, previous works have shown the strong effect of the observational cadence on the determination of the rotation period (Ďurech et al. 2022). Second, the determined period only corresponds to the synodic rotation period ($\mathtt{P}_{\rm syn}$) of the SSO as observed from Earth and not its sidereal rotation period ($\mathtt{P}_{\rm sid}$).

We used the `nifty-ls` implementation of Lomb–Scargle (Garrison et al. 2024), providing a performance boost of almost two orders of magnitude compared to the traditional algorithm (Press & Rybicki 1989). Because the observations are unevenly sampled in time, some over-sampling of the expected width of each frequency peak is required (VanderPlas 2018). For each SSO, the pseudo-Nyquist frequency (δf) was evaluated (with five sampling points per peak; Schwarzenberg-Czerny 1996; VanderPlas & Ivezić 2015) as

$$\delta f = 5/\Delta T \tag{7}$$

,
with ΔT being the baseline. The frequency limits used for the periodogram are 0.12 and 2.4×10^5 hours, corresponding to a sensitivity to rotation periods between 0.24 and 1.2×10^5 hours (choice based on the distribution of known asteroid rotational periods). However, because the parameter space is large and the computation becomes costly, we adopted a two-step strategy. First, a period search window between 1.2 and 2.4×10^5 hours was used and the Lomb–Scargle periodogram was computed using an increasing number of sine and cosine terms k, from 1 to 4, similarly to the approach proposed by Vavilov & Carry (2025). The F-statistic was then computed for each consecutive pair of periodograms in the following manner:

$$F = \frac{N_{\rm o} - {\rm dof}_{k+1}}{{\rm dof}_{k+1} - {\rm dof}_k} \times \left(\frac{{\rm rms}_k^2}{{\rm rms}_{k+1}^2} - 1 \right) \tag{8}$$

,
where $N_{\rm o}$ is the number of data points used in the fit, dof the degrees of freedom, and RMS is the RMS residuals. The indices k and $k+1$ indicate the number of terms of the two compared periodograms. Finally, the degrees of freedom were computed as $2k + 1 + 3N_F$, with N_F being the number of filters used in the photometric data.

To assess whether the increase in model complexity ($k \to k+1$) is statistically justified, we compared the measured F value to a critical threshold α_F derived from the F-distribution. This critical value corresponds to the 99$^{\rm th}$ percentile of the distribution. A more complex model $k+1$ was retained only if $F > \alpha_F$. If this condition was not satisfied, the improvement in the fit was not considered significant at the 1% level, and the simpler model k is preferred, according to the Occam's razor rule. If more than $k = 4$ terms provide a statistically significant improvement to the fit, we consider that no period in the range $1.2 - 2.4 \times 10^5$ hours describes the variability in the data. In the aforementioned case, we repeated this F-test procedure on shorter periods in the $0.12 - -1.2$ hour range. The procedure was repeated in this two-step manner because the period search in the very-high-frequency space takes significantly longer.

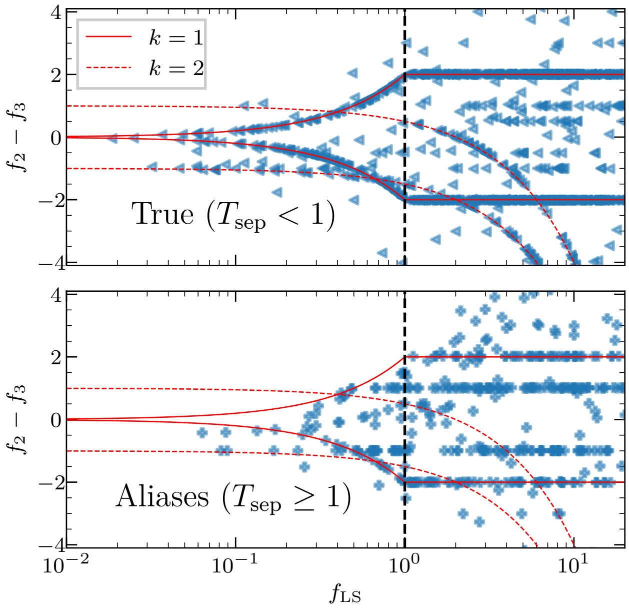

Fig. 3: Difference between the second and third highest periodogram peaks, $f_2 - f_3$, as a function of the observed frequency, $f_{\rm LS}$. The red curves show the analytical relations expected for true frequency evaluations from Eq. 12: solid lines correspond to the $k = 1$ relation, while dashed lines correspond to $k = 2$. *Top*: Solutions identified as true periods. The majority of the points follow the relations of Eq. 12. *Bottom*: Solutions identified as aliases. Most of the frequency differences ($f_2 - f_3$) do not follow the predicted relations. The vertical dashed line indicates the feature frequency, i.e., the 24 h observational cadence.

4.2. Identifying true periods from aliases

The periodogram typically exhibits a dominant peak, which may correspond to the true synodic period, one of its aliases, a period linked with the cadence of observations, or simply a noise-driven outlier. Given the extreme sensitivity of the photometric model to the initial period evaluation (Fig. 2), a method is required to identify in which category the period evaluation falls.

We implemented a test based on a bootstrap technique inspired by a previous analysis of ATLAS sparse photometry (Ďurech et al. 2022). We kept the temporal sampling fixed while each bootstrap realization was generated by randomly drawing (with replacement) a set of photometric measurements from the original dataset. For each resampled dataset, the period search was repeated on the corresponding residuals.

A key distinction from earlier studies is that the periodograms are computed using the residuals of the $\texttt{sHG}_1\texttt{G}_2$ photometric model rather than the raw light curves. This choice ensures that the variability of the signal due to the varying aspect angles in different apparitions are removed by the model, leaving only signatures introduced by the intrinsic rotation and the observational cadence. Therefore, a simple Lomb–Scargle periodogram is enough to find the period, without performing a full modelization of the SSO, saving significant computation time. We generated a total of 25 bootstrap realizations and records for each period for the highest periodogram peak. For the i-th bootstrap sample, we computed the relative deviation

$$\Delta P = \frac{|P_{{\rm BS},i} - P_{\rm LS}|}{P_{\rm LS}} \tag{9}$$

,
where $P_{\rm LS}$ denotes the period associated with the dominant peak in the periodogram of the original residuals and $P_{{\rm BS},i}$ is the corresponding bootstrap estimate. The bootstrap score, N_{BS}, was then defined as the number of bootstrap samples satisfying $\Delta P \leq 0.01$ providing a measure of the period's evaluation stability (chosen here at 1%).

The observing window and its harmonics, which are typically observed at 24 hours, and its perfect divisors and multiples, are responsible for creating strong aliases in the periodogram. The observing window is a secondary periodic signal in the time series of the residuals due to the observation cadence of the telescope, which is convolved with the primary asteroid's spin-period signal, giving rise to the multiple peaks around the true periodic signal. Nonetheless, the strongest peak in the periodogram is not necessarily due to the asteroid's spin, but it can be one of the features described above. In general, the peak of the periodogram is given by

$$f_{\rm LS} = \frac{1}{P_{\rm LS}} = \frac{i+1}{\mathsf{P}_{\rm syn}} \pm \frac{j}{24\ \text{hours}}, \quad i, j > 0 \tag{10}$$

.

To discriminate between true rotational frequencies and aliases produced by the observing window, we adopted a flagging scheme based on the relative location and ordering of the strongest peaks in the periodogram. Let $f_{\rm LS} = 1/P_{\rm LS}$ be the frequency corresponding to the highest peak of the Lomb–Scargle periodogram, and let $f_{\rm feat}$ denote the characteristic frequency of the observing window. In practice, $f_{\rm feat}$ is typically associated with the 24-hour cadence. We further define the peak distance

$$\Delta f_1 = f_2 - f_3 \tag{11}$$

,
where f_2 and f_3 are the frequencies of the second and third highest peaks in the periodogram, respectively. The sign of Δf_1 provides information on the asymmetry of the peak structure around the dominant feature (Fig. 3). The alias-flagging procedure depends on the number of terms, k, selected for the periodogram by the F-test criterion (Eq. 8).

In the case where $k = 1$ we relied on the following assumptions. First, the highest peak in the periodogram corresponds to the true rotational frequency of the asteroid, while aliases induced by the observing window appear as secondary peaks on either side of this frequency in frequency space. Second, we assumed that no additional significant peaks are produced by harmonics of the rotational signal itself, such that the secondary structure of the periodogram is dominated by window-induced aliases.

In the case where $k = 2$, we again assumed that the highest peak in the periodogram corresponds to the true rotational frequency of the asteroid. The highest peak corresponds to the first harmonic, and the second highest peak is the fundamental, at $f_{\rm LS} = 2 f_{\rm true}$. The third highest peak can then be on either side of the highest peak of the periodogram. These assumptions are driven by the visual inspection of numerous periodograms produced using our simulated dataset.

Using these assumptions, one can find the following diagnostic quantity, T_k, from Eq. 10 as

$$T_k = \begin{cases} +2f_{\rm feat}, & k=1,\ \ \Delta f_1 > 0 \ \text{and} \ f_{\rm LS} > f_{\rm feat}, \\ -2f_{\rm LS}, & k=1,\ \ \Delta f_1 < 0 \ \text{and} \ f_{\rm LS} < f_{\rm feat}, \\ +2f_{\rm LS}, & k=1,\ \ \Delta f_1 > 0 \ \text{and} \ f_{\rm LS} < f_{\rm feat}, \\ -2f_{\rm feat}, & k=1,\ \ \Delta f_1 < 0 \ \text{and} \ f_{\rm LS} > f_{\rm feat}, \\ -0.5f_{\rm LS} - f_{\rm feat}, & k=2,\ \ f_2 > f_{\rm LS}, \\ -0.5f_{\rm LS} + f_{\rm feat}, & k=2,\ \ f_2 < f_{\rm LS} \end{cases} \tag{12}$$

.
Whether a peak is an alias or not is then quantified by the distance between the measured peak separation and the expected peak separation under the assumption that the peak corresponds to the true signal:

$$T_{\rm sep} = 100\ |\Delta f_1 - T| \tag{13}$$

If $T_{\rm sep} < 1$, the periodogram peak is classified as a true rotational period. Otherwise, the peak is flagged as an alias induced by the observing window. The success rate of the flagging scheme is listed in Table 1.

We reiterate that the alias flagging method is based on the assumption of a dominant 24 hour observational cadence, which is representative of most ground-based surveys. Nevertheless, adopting a different cadence would primarily modify the method quantitatively rather than conceptually, provided that Eq. 10 remains valid. This condition is satisfied for the vast majority of period analyses performed with the Lomb–Scargle periodogram, meaning that the approach can in principle be adapted to other surveys, including combined datasets, by recalibrating the corresponding T_k values of Eq. 12 for the relevant cadence structure.

4.3. From the synodic to the sidereal period

The Lomb–Scargle periodogram provides an average synodic period of $\mathtt{P}_{\rm syn}$. The relevant quantity required to tie all observations together is the sidereal period, $\mathtt{P}_{\rm sid}$, which is defined in an inertial frame. The two periods can differ by tens of seconds for a typical period of a few hours. Their difference is a multivariate quantity that depends on the semimajor axis of the asteroid, its spin axis orientation and its sidereal period itself. Considering that the sub-observer longitude between two observations, A and B, separated by exactly one synodic period (such as $t_B = t_A + \mathtt{P}_{\rm syn}$), differ by 2π by definition, one finds

$$\mathtt{P}_{\rm sid} = 2\pi \mathtt{P}_{\rm syn} / (W_A - W_B)\ , \tag{14}$$

,
where W_i are functions of the coordinates of the target and its spin axis (Eq. A.13). The difference between the synodic and sidereal periods is therefore not fixed, it depends on the period itself and the apparent motion of the target. Those located closer to the observer exhibit a larger apparent motion on the sky over one synodic period; hence, there is a larger difference between $\mathtt{P}_{\rm syn}$ and $\mathtt{P}_{\rm sid}$.

We explored this difference by randomly selecting 100 SSOs with evenly spaced semimajor axes of between 0.5 and 10 au. For each one, we used the `Miriade` ephemeris service[2] (Berthier et al. 2008) to compute their apparent positions on sky every two days for two full orbital periods. For each trial sidereal period, $\mathtt{P}_{\rm sid}$, we computed the sub-observer longitudes φ_i at each propagated epoch and derived the corresponding synodic periods (Eq. 14).

The absolute difference between $\mathtt{P}_{\rm syn}$ and $\mathtt{P}_{\rm sid}$ at each epoch quantifies the de-phasing caused by the combined motion of the SSO and the observer. To capture the effect of varying spin properties, we repeated this calculation over a grid of $\alpha_0 \in [0^{\rm o}, 360^{\rm o}[$ with steps of $10^{\rm o}$, $\delta_0 \in [-90^{\rm o}, 90^{\rm o}]$ every $5^{\rm o}$, $\mathtt{P}_{\rm sid} \in [1\,{\rm h}, 10^3\,{\rm h}]$, with 25 logarithmically spaced steps. For each of the 1250 combinations of semimajor axis, sidereal period, and spin-axis coordinates, we recorded the median of the absolute deviation between synodic and sidereal period (for all epochs) as shown in the top left panel of Fig. 4.

We then computed the maximum period deviation ($\Delta P_{\rm max}$) for each semimajor axis (top left panel of Fig. 4). We used this to determine the sample of sidereal periods to be tested from the synodic period found by Lomb–Scargle analysis. Specifically, for a survey of duration $T_{\rm survey}$, the uncertainty in resolving a period of $\mathtt{P}_{\rm sid}$ can be approximated as

$$\Delta P_{\rm LS} \sim \frac{1}{2}\frac{\mathtt{P}_{\rm sid}^2}{T_{\rm survey}} \tag{15}$$

,
which represents the minimal detectable difference between aliases (Kaasalainen & Torppa 2001). The number of samples is then given by the ratio of the maximum period deviation and the period resolution ($\Delta P_{\rm max}/\Delta P_{\rm LS}$).

Furthermore, the magnitude of this synodic–sidereal difference increases with the sidereal period itself (Eq. 14). Slower rotators accumulate a larger phase offset over the same observing baseline, amplifying the discrepancy between the synodic and sidereal solutions. Both effects are reproduced by our simulations, which show that the maximum expected period difference scales quadratically with the sidereal period for a given semimajor axis. This behavior follows the empirical relation

$$\log_{10}|P_{\rm synodic} - P_{\rm sidereal}| = 2\ \log_{10} P_{\rm sidereal} + \beta \tag{16}$$

,
where the slope is fixed and consistent across all simulated objects, while the intercept, β, depends solely on the semimajor axis of the target.

Both the maximum expected difference between the two periods and the number of distinct intervals (N) that must be explored around the synodic solution therefore depend on the semimajor axis of the object (a). To capture this dependence, we fitted these quantities as shown in the bottom panels of Fig. 4 and derived the characteristic width of these intervals (in hours) as

$$N(a) = 71.073\, e^{-1.21a} + 2.528, \tag{17a}$$

$$\beta(a) = 1.619\, e^{-0.338a} - 5.069, \tag{17b}$$

$$W(a) = 10^{\,2\log_{10}\mathtt{P}_{\rm sid} + \beta(a)}. \tag{17c}$$

[2] https://ssp.imcce.fr/webservices/miriade/

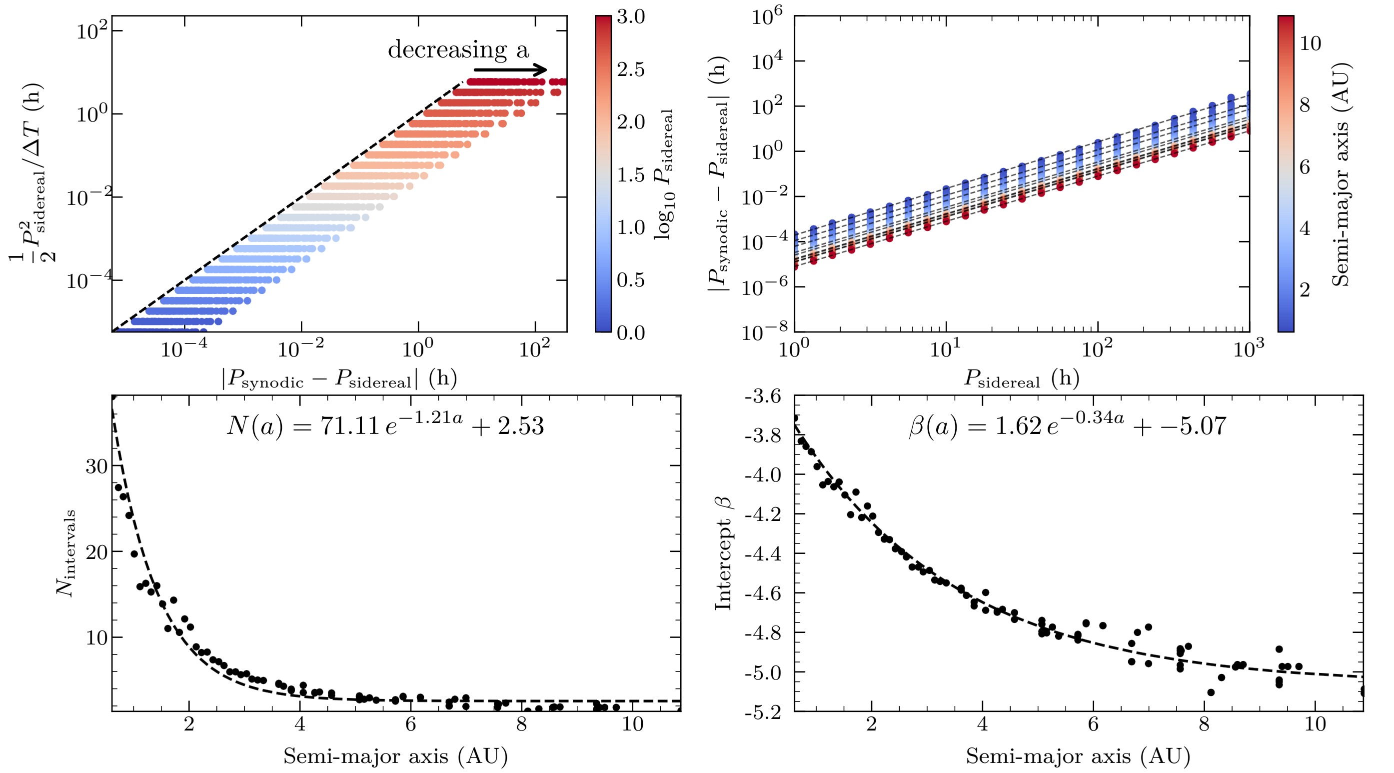

Fig. 4: Procedure for defining the synodic–sidereal period window and the number of resolvable period intervals as a function of semimajor axis. *Top left*: For each semimajor-axis slice, the maximum synodic–sidereal period offset, $|P_{\rm syn} - P_{\rm sid}|$, is compared to the Lomb–Scargle periodogram resolution limit, $\frac{1}{2}P^2_{\rm sid}/\Delta T$, where ΔT is the ten-year observational baseline. Points are color-coded by $\mathtt{P_{sid}}$ and the black line marks the 1:1 line. *Top right*: Maximum resolvable synodic–sidereal offset as a function of sidereal period for each semimajor-axis slice. Dashed lines show power-law fits of the form $\log_{10}|P_{\rm syn} - P_{\rm sid}| = 2\log_{10} P_{\rm sid} + \beta$, with color indicating semimajor axis. *Bottom left*: Number of resolvable period intervals, $N_{\rm intervals} = |P_{\rm syn} - P_{\rm sid}|/(\frac{1}{2}P^2_{\rm sid}/\Delta T)$, as a function of semimajor axis, with an exponential approximation. *Bottom right*: Fitted intercept, β, as a function of semimajor axis, also modeled by an exponential decay.

.

The method still requires an accurate initial synodic period estimate, as an incorrect solution would propagate to the explored intervals to the detriment of the ellipsoidal shape modeling. An incorrect initial guess of the period would lead to a de-phasing of the light curve over the observations made around the reference epoch. The final derived parameters, such as shape and spin-axis coordinates, would be unreliable. Therefore, the ability to retrieve an accurate synodic period estimate from the provided light curves can be seen as a minimum requirement for a SOCCA inversion.

4.4. Recovering true periods from aliases

We tested the solutions flagged as aliases (Eq. 12) to recover possible true periods. For cases with $k = 1$, we repeated two SOCCA fits with trial frequencies $f_{\rm obs} \pm f_{\rm feat}$. For cases with $k = 2$, we repeated one SOCCA fit with a trial frequency of $2f_{\rm obs}$. These trial periods were computed as previously done (Eq. 10).

For each solution we computed the $\mathtt{sHG_1G_2}$ forward model using the SOCCA fit parameters and determined the sub-Earth longitude (Eq. A.13). We subtracted the $\mathtt{sHG_1G_2}$ model from the data and phase-folded the residuals over the sub-Earth longitude, producing a double-peaked light curve. We then used the Θ statistic from Stellingwerf (1978) to select the true rotational frequency via phase-dispersion minimization:

$$\Theta = \frac{S^2}{\sigma^2}, \tag{18}$$

$$\sigma^2 = \frac{\sum_{i=1}^{N}(x_i - \bar{x})^2}{N-1}, \tag{19}$$

$$S^2 = \frac{\sum_{j=1}^{M}(n_j - 1)s_j^2}{\sum_{j=1}^{M} n_j - M} \tag{20}$$

, where σ^2 is the total variance of the magnitudes, x_i, and S^2 is the variance of the $M = 100$ samples containing n_j points with a variance of s_j. The trial period for which Θ is closest to unity was selected as the true rotational period.

5. Validation on simulated data

5.1. Simulating LSST-like data

We used SORCHA (Merritt et al. 2025) to generate simulated light curves for 500 SSOs for each of the following ten dynamical classes: Aten; Amor near-Earth asteroids, Apollo near-Earth asteroids, Mars-crossers, the inner main belt, the middle main belt, the outer main belt, Jupiter trojan, Centaurs, and KBOs. The orbital parameters correspond to the actual parameters of the sampled objects, while the physical parameters are randomly drawn from physically motivated distributions accessed with the `rocks`[3] python client of `SsODNet` (Berthier et al. 2023). The absolute magnitude, H, was sampled from a uniform distribution bounded by the minimum and maximum values of the observed H distributions for each dynamical class. The spin period is drawn from the observed spin-period distribution of the entire SSO population, with the exception of near-Earth asteroids, for which a separate distribution is used; it is characterized by systematically shorter periods. The spin-axis coordinates α_0 and δ_0 were sampled from the observed distributions of SSOs. The shape parameters `a/b` and `a/c` were taken from the `DAMIT` database of three-dimensional shape models, while enforcing the ordering `a/b` < `a/c`.

The only exceptions here are the G_1 and G_2 phase parameters and the LSST colors required by SORCHA. The phase parameters were selected according to the taxonomic class of the sampled objects using the scheme from Mahlke et al. (2021). The LSST colors ($u-r$, $g-r$, $i-r$, $z-r$, $y-r$) were computed[4] using the prototype spectra from Mahlke et al. (2022) and using filters' transmission curves[5] (Rodrigo et al. 2012; Rodrigo & Solano 2020).

Using these parameters, SORCHA simulates[6] the photometric time series (Eq. 1) and samples the resulting light curves as they would be observed by the LSST over a ten-year baseline. From the simulated catalog, we only retain objects that have at least 50 observations in at least one filter, ensuring sufficient photometric coverage for a meaningful inversion. Out of the 5,000 total sampled objects, 2,816 were observed by the simulated LSST survey and 2,207 were selected after having more than 50 observations. The selected objects were then analyzed using the SOCCA model.

5.2. Success rate

We applied SOCCA to 2,207 objects with a resulting success rate of 52.8%. Of these 2,207 objects, 17 failed because $\mathtt{sHG_1G_2}$ did not converge, and four failed because SOCCA did not converge. In addition, 500 objects were flagged as having unreliable period estimates from the bootstrap criterion (Eq. 9). A further 304 objects produced shapes for which `a/b` and `a/c` differed by less than 1%, indicating that the `a/c` axis of the ellipsoid is poorly constrained.

Additionally, 42 solutions returned nonphysical values of G_1 or G_2: For each model and each filter, we evaluated the number of successful solutions, defining a solution as valid when the G_1 and G_2 parameters were within $> 5 \times 10^{-3}$ of the bounds given in Eqs. 4a to 4c. Solutions that do not satisfy these conditions are considered nonphysical, as they approach the bounds of the parameter space. This behavior in the optimization algorithm is a sign of poor constraints on the phase-curve parameters from the data. Finally, 175 objects failed due to more than one of the failure modes listed above being true simultaneously, as the conditions are not mutually exclusive. The metrics above encompass the

[3] https://rocks.readthedocs.io
[4] https://github.com/bcarry/ska
[5] https://svo2.cab.inta-csic.es/theory/fps/
[6] Available to everyone using the `ellipsoidalWithTerminator` light-curve module; we provided to SORCHA add-ons: https://sorcha-addons.readthedocs.io

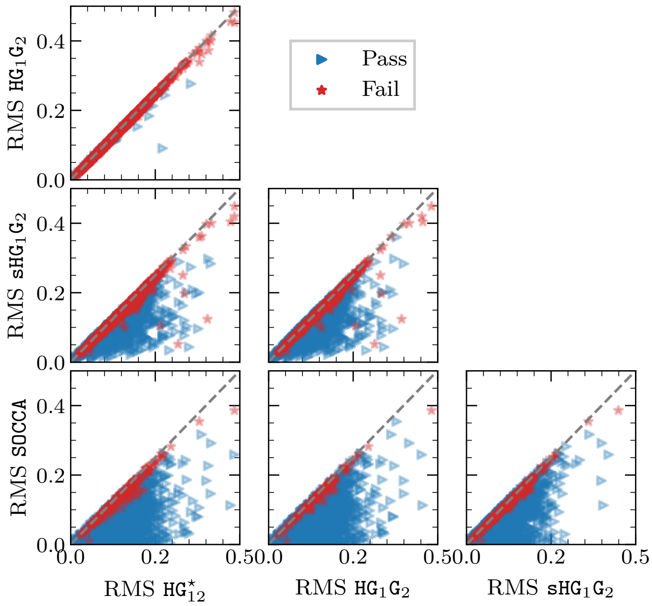

Fig. 5: Comparison of RMS between the different photometric models. The gray line represents the 1:1 line, where no improvement in the RMS is observed between models. The blue triangles depict the inversions for which the more complex model (with more free parameters) is justified by a statistically significant improvement in the residuals (Eq. 8). Conversely, the red stars represent those for which the simpler model is more relevant.

criteria for a successful SOCCA solution. They quantify the requirements of sufficient phase- and aspect-angle coverage as well as adequate sampling of the light curve to retrieve the rotational period. They can be implemented without the requirement of any previous knowledge of the target SSO physical properties.

Only a limited number of objects were recovered with the $\mathtt{HG_1G_2}$ model, the dominant limitation being the unmodeled effect of shape. This limitation is mitigated with both $\mathtt{sHG_1G_2}$ and SOCCA, with the inclusion of the shape and the shape-spin-induced variability, respectively. As a consequence, we recovered an additional ∼10–20% of valid solutions per filter with SOCCA when compared to $\mathtt{HG_1G_2}$.

5.3. Computational cost and scalability

The application of SOCCA to the simulated sample of 2,207 objects allowed us to directly quantify the computational cost of the inversion. The distribution of inversion times is shown in Fig. 7. The median runtime is ∼157 s per object, with 30% of the solutions converging in less than ∼87 s and 90% in less than ∼416 s on a single core.

The inversion time scales with the number of observations, as expected from the least-squares minimization. This trend is visible in Fig. 7, where the runtime increases approximately linearly with the number of data points. Most solutions are obtained within a few minutes, and the majority remain well below one hour.

Overall, the method scales well with the size of the dataset, and can be applied to several thousand objects with modest computational resources. This makes it di-

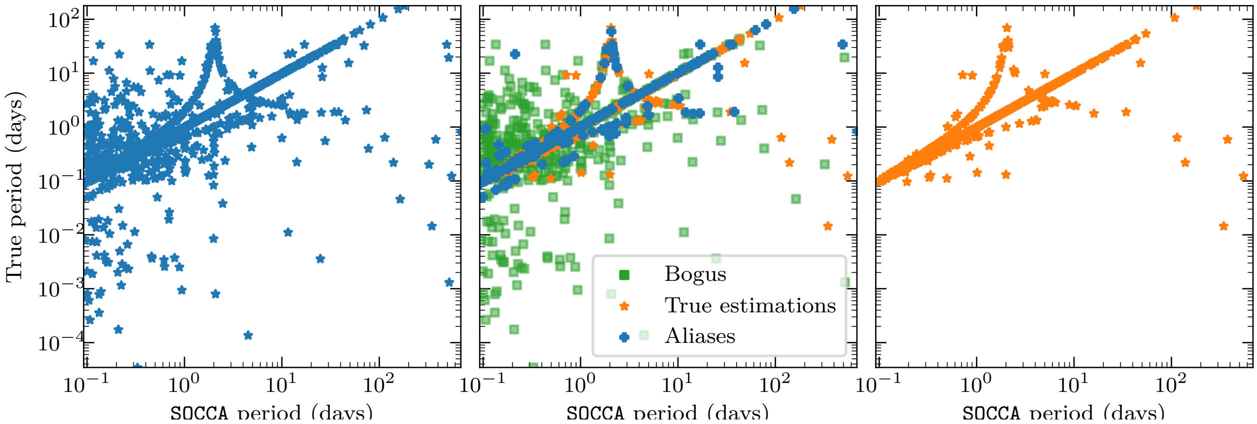

Fig. 6: Comparison between simulated and retrieved periods for each simulated SSO. *Left*: Period estimates from the Lomb–Scargle periodogram. Both alias branches are visible above and below the 1:1 line, as well as the double-period harmonic below and parallel to the 1:1 line. *Center*: Application of our quality flags. Green squares indicate low-scoring samples (Eq. 9), while blue crosses mark estimates flagged as aliases by the criterion of Eq. 12. *Right*: Final estimates after removing bogus solutions and applying the phase-dispersion-minimization step.

rectly applicable to current surveys such as ZTF and suitable for the larger datasets expected from LSST.

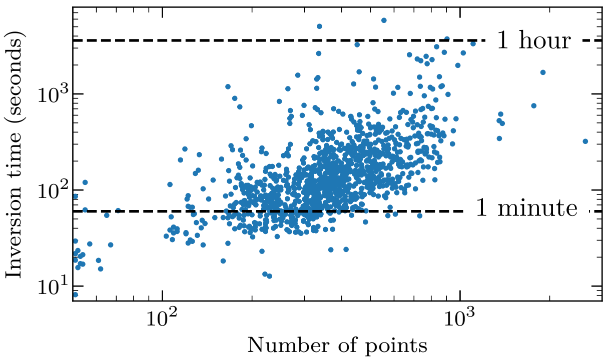

Fig. 7: Inversion time as a function of the number of observations. The horizontal lines indicate one minute and one hour. Most solutions are obtained within a few minutes, with a clear dependence on the number of data points.

5.4. Fit residuals

As shown by Carry et al. (2024), the $\texttt{sHG}_1\texttt{G}_2$ model returns systematically lower RMS values than both HG and $\texttt{HG}_1\texttt{G}_2$ as it accounts for the variations in brightness induced by changes in the viewing geometry. This behavior is confirmed here on SORCHA simulations, with RMS values significantly reduced with respect to HG and $\texttt{HG}_1\texttt{G}_2$ but not fully reaching the expected observational uncertainty of σ. This indicates that while a substantial fraction of the photometric variability is captured by $\texttt{sHG}_1\texttt{G}_2$, an un-modeled source of scatter in the light curve remains due to the rotation of the object. This is captured by SOCCA, translating into a further reduction of the RMS with respect to all previous models. The SOCCA model provides much lower fit residuals with respect to previous models, with a mean RMS of $_{\texttt{SOCCA}} = 0.07$, compared to $\text{RMS}_{\texttt{sHG}_1\texttt{G}_2} = 0.11$ and $\text{RMS}_{\texttt{HG}_1\texttt{G}_2} \approx \text{RMS}_{\texttt{HG}^\star_{12}} = 0.14$. Similarly, for the median reduced chi-squared, $\chi^2_{\nu,\texttt{SOCCA}} = 8.81$, while $\chi^2_{\nu,\texttt{sHG}_1\texttt{G}_2} = 61.9$ and $\chi^2_{\nu,\texttt{HG}_1\texttt{G}_2} \approx \chi^2_{\nu,\texttt{HG}^\star_{12}} = 108.9$.

SOCCA introduces a total of $3N_F + 6$ free parameters, with N_F being the number of bands, which is significantly more than the $2N_F$ parameters of HG or the $3N_F$ of $\texttt{HG}_1\texttt{G}_2$. We hence tested whether the success of SOCCA is due to an excessive number of parameters. We adopted a hierarchical modeling strategy in which the models are evaluated from the simplest to the most complex formulation. The final choice was made using the F-test (Eq. 8), so the most frugal model that provides a statistically significant improvement in the fit is retained. Therefore, each increase in model complexity must correspond to a measurable gain in descriptive power. Even under this constraint, 88.5% of the inversions tested here pass the F-test between all tested models and SOCCA (Fig. 5). The failure of $\texttt{HG}_1\texttt{G}_2$ and $\texttt{HG}^\star_{12}$ therefore reflects an incomplete physical description rather than over-parameterization. In this context, degrading the phase-function formulation from $\texttt{HG}_1\texttt{G}_2$ to simpler variants such as $\texttt{HG}^\star_{12}$ does not address the underlying issue. The appropriate response is to improve the physical description of the model, as done here with SOCCA.

5.5. *H*, G_1, and G_2

We compared the absolute magnitude H and the phase-function parameters $\texttt{G}_1$ and $\texttt{G}_2$ retrieved by SOCCA and the other photometric models with the simulation inputs. First, SOCCA precisely and accurately retrieved the absolute magnitude (Fig. 8). The average difference between the simulated and computed H is of 0.001 mag only, and the scatter (i.e., the uncertainty) is nearly three times smaller than with other models. The offset seen in $\texttt{HG}_1\texttt{G}_2$ is due to the updated definition of H; see Sect. 2.

Second, SOCCA also retrieves the phase-function parameters more precisely and accurately than other models (Fig. D.1). The average difference between the simulated and estimated $\texttt{G}_1$ and $\texttt{G}_2$ are about 0.03 on average, an improvement of a factor three compared to previous models for G_1. The dispersion is significantly reduced with SOCCA (about half that of HG_1G_2; it is around 0.3 and 0.2 for G_1 and G_2, respectively. This results in a much more informative G_1G_2 plane: from HG_1G_2 to sHG_1G_2 to SOCCA, the distribution becomes sharper, allowing us to clearly separate, for example, the S- and C-type populations with SOCCA (Fig. D.1).

5.6. Spin-axis orientation

From the derived spin coordinates (α_0, δ_0), we computed the obliquity of each target and compared it with the simulated obliquity (Fig. 9). 68.5% of the solutions lie within 15° of the true value. Of the remaining 31.5% of the failures, 25.5% correspond to either incorrect period estimates or limited phase-angle coverage ($< 15°$). The erroneous obliquities are not randomly distributed and largely correspond to mirror spin solutions (i.e., α_0 +180°, -δ_0).

5.7. Rotational period

To evaluate the performance of the period classification, we used the F_β score (Goutte & Gaussier 2005), which allows different weights to be assigned to purity and completeness. A small value of β places more importance on purity; therefore, we adopted $\beta = 0.25$.

To identify bogus period estimates we applied a cutoff to the bootstrap score (Sect. 4.2). The optimal threshold was found by maximizing F_β, resulting in a selected cutoff of nine (Fig. 10). We also identified the first-order aliases and the doubling of the true frequency, as illustrated in Fig. 6, which were then re-evaluated with phase-dispersion minimization (Sect. 4.4). With these quality cuts and corrections, the purity of the true-period sample increased from 60.4% to 75.8%. The overall performance of the classification is summarized in Table 1.

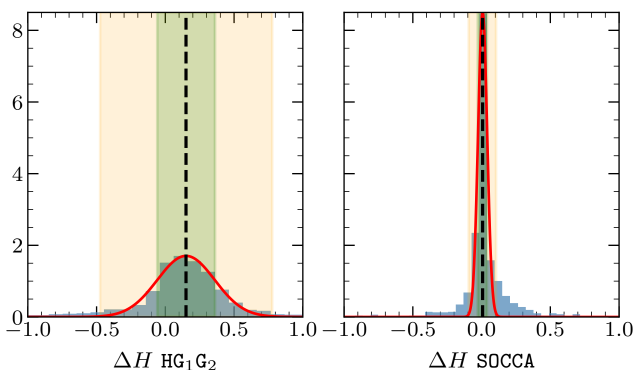

Fig. 8: Difference between simulated and computed H for HG_1G_2 and SOCCA. Gaussian fits to the distributions are shown. The HG_1G_2 residuals have a mean of 0.150 with $1\sigma = 0.209$ and $3\sigma = 0.626$, while SOCCA shows a significantly tighter distribution with a mean of 0.008, $1\sigma = 0.033$, and $3\sigma = 0.099$.

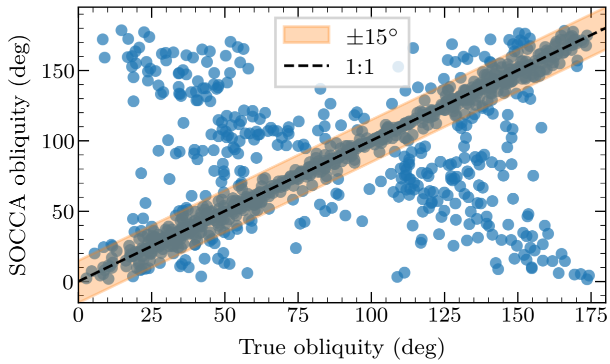

Fig. 9: Input versus output spin axis obliquity of the sampled SSOs. The orange area represents the ±15° we consider as a successful estimate

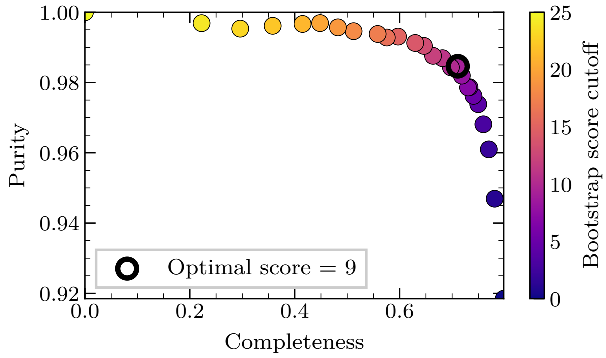

Fig. 10: Purity and completeness as a function of the bootstrap-score threshold used to identify bogus period estimates. The selected cutoff of nine maximizes the F_β score with $\beta = 0.25$.

Table 1: Purity and completeness of each period class.

	Purity (%)	Completeness (%)	TP	FP	FN
True	75.8	83.7	1134	362	220
Alias	41.4	25.5	128	181	373
Bogus	41.6	84.1	296	415	56

Notes. Purity and completeness of each period class along with the number of true-positive (TP), false-positive (FP), and false-negative (FP) period estimates.

5.8. Shape

We compared the axis ratios a/b and a/c obtained from the model with the values used in the simulated sample. A solution is considered successful if the retrieved value lies within 20% of the sampled value.

Using this criterion, we obtained a success rate of 83.3% for a/b and 67.4% for a/c (Fig. 11). The higher success rate for a/b is expected, as this axis ratio is mainly constrained by the spin-induced amplitude of the light curve. In contrast, a/c is constrained through changes in the aspect angle, which require observations spanning a wide range of viewing geometries, in particular the aspect angle. Such

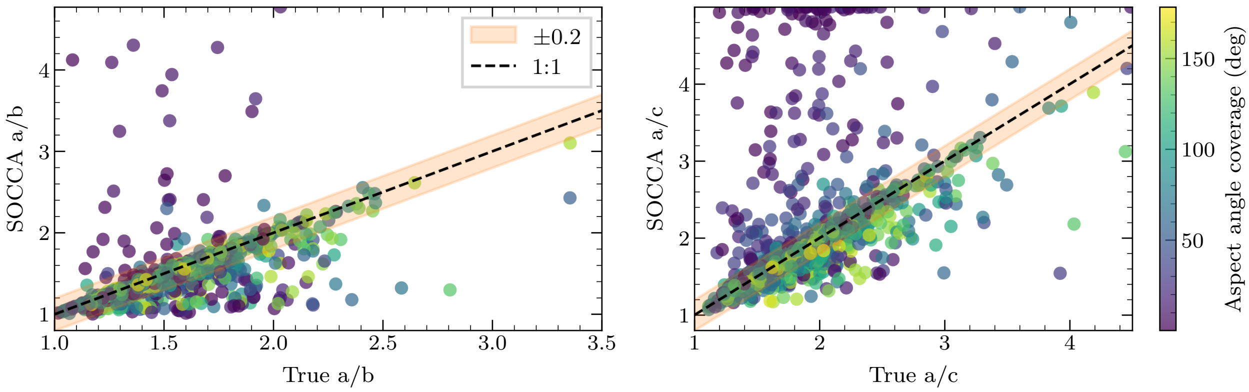

Fig. 11: Comparison between the sampled and retrieved axis ratios `a/b` and `a/c`. The orange area indicates the ±20% region used to define successful solutions.

coverage is not always available in the dataset, leading to a lower recovery rate.

6. Validation on real data

We evaluated the performance of the model on real observations. We applied `SOCCA` to the asteroid (45) Eugenia, using photometric measurements obtained by the ZTF (Masci et al. 2019). The dataset consists of 265 photometric measurements acquired between 2019-11-09 and 2026-02-23. The observations were retrieved from Fink (Möller et al. 2021) and distributed in the g and r filters.

We compared the results with the $\mathtt{HG_1G_2}$ and $\mathtt{sHG_1G_2}$ model. The `SOCCA` solution produces significantly smaller residuals, as seen in Fig. 12, indicating a better description of the observed brightness variations. More specifically, we retrieved a sidereal rotational period of 5.699,136 hours, compared to 5.699,152 hours obtained from 3D shape reconstruction using light curves and adaptive-optics images (Vernazza et al. 2021). Similarly, we derived spin axis coordinates of $(\alpha_0, \delta_0) = (119^{+2}_{-2}, -19^{+5}_{-5})^{\mathrm{o}}$, while the 3D shape reconstruction returns $(\alpha_0, \delta_0) = (121^{+2}_{-2}, -16^{+2}_{-2})^{\mathrm{o}}$ only 4^{o} away. Finally, the reported shape axis ratios are $\mathtt{a/b} = 1.319^{+0.08}_{-0.08}$ and $\mathtt{a/c} = 1.826^{+0.11}_{-0.11}$, whereas `SOCCA` retrieves $\mathtt{a/b} = 1.366^{+0.03}_{-0.03}$ and $\mathtt{a/c} = 2.165^{+0.16}_{-0.16}$.

We further validated the model using dense light curves of (45) Eugenia available in the `DAMIT` database. The `SOCCA` model was propagated to the epochs corresponding to the dense-light-curve observations and directly compared with the measured magnitudes. In most cases, the model reproduces the dense light curves well, as seen in the top plot in Fig. 13, where we compare with a dense light curve taken in 2014 (Hanuš et al. 2016). Deviations are expected because (45) Eugenia is not a perfectly symmetric triaxial ellipsoid, while the model assumes such a geometry. Certain viewing configurations therefore produce systematic offsets between the predicted and measured brightness (Fig. 13, middle). Additional discrepancies arise from small differences in the sidereal rotation period. The period derived by `SOCCA` differs from the value reported in `DAMIT` by approximately 0.03 seconds. Over long time baselines this leads to a gradual phase drift. As a result, light curves obtained many years before the ZTF observations show a measurable phase shift. For example, the dense light curve obtained in 1978 (Debehogne & Zappala 1980) is offset by roughly 88% of one rotation cycle when compared with the propagated model.

7. Discussion

The formulation presented here assumes a triaxial ellipsoidal shape in principal-axis rotation. In this configuration, the model captures the photometric variability induced by the shape and the rotation in tandem with the phase-angle variations.

This assumption can be modified without changing the overall structure of the approach. For objects with irregular shapes, or non-principal-axis rotation, the description of the rotational signal can be substituted with, for example, cellinoid (Lu et al. 2014), tumbling rotation (Kaasalainen 2001), or a full 3D model (Kaasalainen & Torppa 2001), still benefitting from the efficient search of the initial conditions.

Another line of extension of `SOCCA` includes the binary systems, which introduce additional variability through mutual eclipses and occultations (Scheirich & Pravec 2009). These events alter the observed flux at specific epochs and are not captured by a single-body description. Modeling such systems requires accounting for the orbital configuration and the relative properties of the components. Similarly, for the case of active asteroids and comets, the observed signal includes a contribution from the surrounding material, which can vary independently of the rotational phase.

Overall, the formulation presented here provides a baseline that is well suited for the vast majority of SSOs. More complex situations can be addressed by extending the model, at the cost of additional parameters.

Another interesting implementation of `SOCCA` is that of identifying candidates for follow-up observations. The number of candidates within SSOs is expected to increase dramatically with the advent of LSST, while the resources needed to conduct more detailed dense-light-curve observing campaigns remains limited. The identification of interesting signatures in the `SOCCA` model residuals (e.g., periodic deviations from the ellipsoid shape) can lead to some kind of target prioritization.

We also note the fact that LSST will observe a significant number of SSOs (5.3 million discoveries), but with

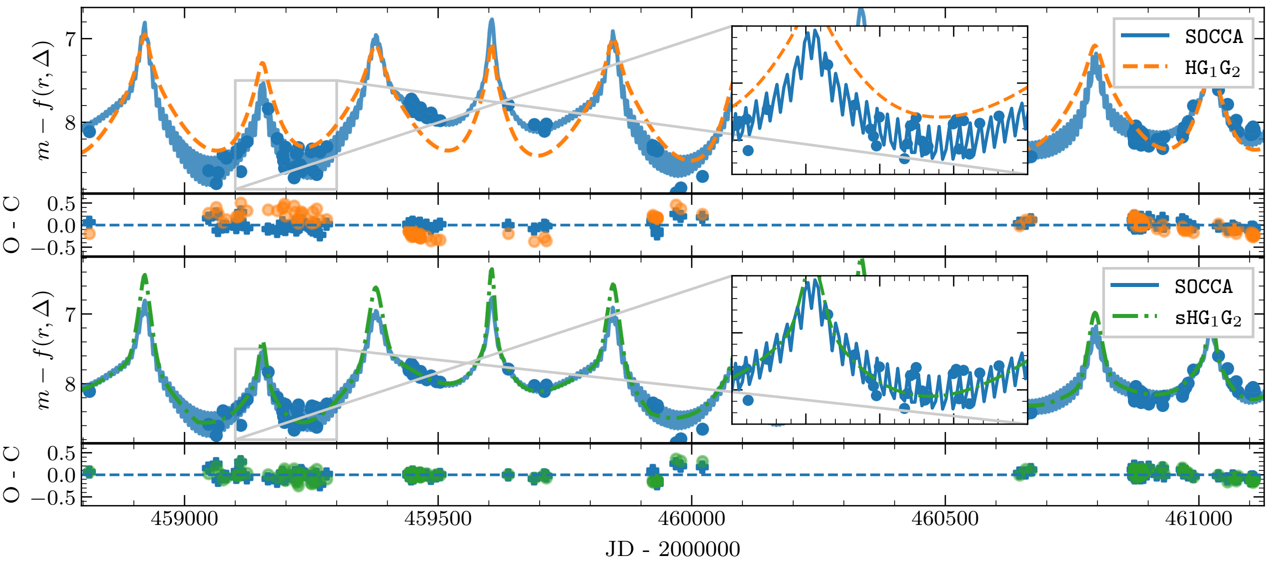

Fig. 12: Comparison between SOCCA, HG_1G_2, and sHG_1G_2 model fitting for (45) Eugenia. The large panels show the model prediction versus the observations obtained by ZTF in the g filter over the approximately ten-year baseline, and the smaller panels show the difference between the model prediction and the observations. In the top pair of panels the SOCCA- HG_1G_2 comparison is shown, and in the bottom pair we show the SOCCA- sHG_1G_2 comparison. In the insets, the high-frequency signal due to the rotation of the asteroid is shown, which is modeled by SOCCA, but missed by both HG_1G_2 and sHG_1G_2, the latter of which captures the shape variation.

a relatively small median number of observations per object (between 23-234 detections, depending on dynamical class; Kurlander et al. 2025). However, the model is not intended to operate exclusively on LSST photometry. An advantage of the method is its multi-filter design, which allows the combination of data from different surveys into unified light curves. LSST was therefore used here primarily as a reference case and because it is expected to provide some of the highest quality photometric measurements for future combined datasets.

7.1. Model availability

SOCCA is currently being integrated into the SSO scientific pipeline of the FINK alert broker and is expected to provide near-real-time parameter estimates for both ZTF and LSST data streams, which will then be freely available to the scientific community.

The model is publicly available[7] and can be installed as a Python package. It is implemented as an extension of the phunk library for phase-curve fitting[8], and follows the same interface. The user first defines a PhaseCurve object containing the photometric data in array-like format. The arrays should include the reduced magnitude and associated uncertainties, the epoch of each observation, the phase angle, and the corresponding filter. From this, the sub-observer and subsolar coordinates were computed. An initial parameter vector was then constructed following the initialization steps laid out in Sect. 3 and Sect. 4, after which the SOCCA model can be fitted directly. The retrieved parameters are stored as attributes of the phase-curve object. The fitting process is illustrated below:

```python
import phunk
from socca_tune.initialize import initialize

# Phase curve object from photometric data
pc = phunk.PhaseCurve(
    target="Eugenia",
    epoch=data["Date"],  # J2000
    phase=data["Phase"], # degrees
    mag=data["Reduced magnitude"],
    mag_err=data["Photometric errors"],
    band=data["Photometric filter ID"],
)

# retrieve coordinates
pc.get_ephems()

# initialize parameters
p0,_= initialize(pc, weights=pc.mag_err)

# run SOCCA fit
pc.fit(["SOCCA"], p0, weights=pc.mag_err)

# access fitted parameters
pc.SOCCA.alpha  # Spin axis right ascension
pc.SOCCA.delta  # Spin axis declination
pc.SOCCA.period # Sidereal rotational period
```

8. Conclusions

We present SOCCA, a new approach to simultaneously determining the spin, shape, and absolute magnitude (and, hence, colors) of SSOs from photometry such as that pro-

[7] https://github.com/astrockers/socca-tune
[8] https://github.com/astrockers/phunk

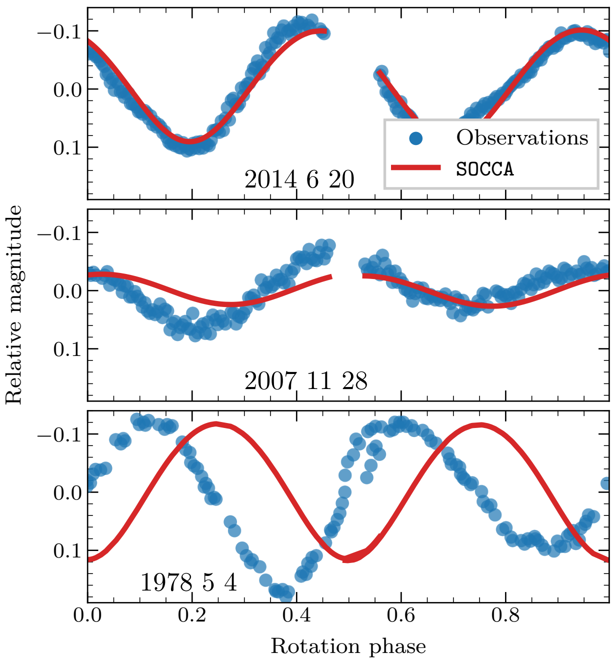

Fig. 13: Comparison between the densely sampled light curves of (45) Eugenia and the `SOCCA` model of the same SSO propagated to the dates of observation. *Top*: Well-reproduced light curve (Hanuš et al. 2016) captured near the observational midpoint of the data used to build the `SOCCA` model. *Center*: Light curve (Marchis et al. 2010) captured under a certain object–observer orientation, leading to an offset in the magnitude axis due to the non-symmetry of the SSO. *Bottom*: Light curve captured significantly earlier than the midpoint of observations (ibid), leading to a visible de-phasing between our model and the observations.

duced nightly by large sky surveys. `SOCCA` is a frugal approach, striving to minimize the number of free parameters. It can be seen as a compromise between simple phase-curve fitting and the derivation of full 3D shape models. We propose a suite of preliminary steps to initialize the model, avoiding computationally expensive approaches such as a grid search.

We validated `SOCCA` based on simulations of LSST-like observations for 2,207 SSOs. `SOCCA` finds a solution in ≈50% of the cases. Among these, `SOCCA` systematically provides a better description of the observations, with significantly smaller residuals. We also validated `SOCCA` on ZTF observations of (45) Eugenia. The parameters determined with `SOCCA` matches those from the more complex 3D shape modeling approach. The magnitudes predicted by `SOCCA` provide a good description of dense light curves, with the limitation of the symmetry imposed by the ellipsoidal shape.

The derived photometric parameters, the phase-function coefficients ($\mathtt{G_1G_2}$), and the absolute magnitude ($\mathtt{H}$) in each filter, and thus colors, are more accurately determined than with previous approaches (e.g., $\mathtt{HG_1G_2}$ modeling). This provides a more robust basis for taxonomic studies of large corpus of data. The physical parameters introduced in `SOCCA`—the sidereal rotation period, $\mathtt{P_{sid}}$; spin-axis coordinates (α_0, δ_0), and the ratios of triaxial ellipsoid diameter (`a/b`, `a/c`)—are accurately retrieved by the algorithm. This provides a new possibility to study the structure and diffusion of dynamical families, governed by these properties through the Yarkovsky effect.

We designed `SOCCA` to be frugal and robust, so it is practically possible to apply it to very large samples, up to several 10^5 SSOs, to shift from individual studies to a population-level description of SSOs. In the context of large surveys such as LSST, such a model is required to handle the volume of data.

Acknowledgements. BC. and KOX. was supported by CNRS/INSU/PNP and CNES APR. We thank these programs for their support. This research used the `Miriade` (Berthier et al. 2008), `SsODNet` (Berthier et al. 2023), and `TOPCAT` (Taylor 2005) Virtual Observatory tools. It used the `astropy`[9] (Astropy Collaboration et al. 2013, 2018, 2022), `sbpy`[10] (Mommert et al. 2019), `rocks`[11] (Berthier et al. 2023), and the Flat-Iron Institute `nifty-ls` (Garrison et al. 2024) python packages. This work was developed within the Fink community and made use of the Fink community broker resources. Fink is supported by LSST-France and CNRS/IN2P3. Thanks to all the developers and maintainers

References

Archinal, B. A., Acton, C. H., A'Hearn, M. F., et al. 2018, Celestial Mechanics and Dynamical Astronomy, 130, 22

Astropy Collaboration, Price-Whelan, A. M., Lim, P. L., et al. 2022, apj, 935, 167

Astropy Collaboration, Price-Whelan, A. M., Sipőcz, B. M., et al. 2018, AJ, 156, 123

Astropy Collaboration, Robitaille, T. P., Tollerud, E. J., et al. 2013, A&A, 558, A33

Bartczak, P. & Dudziński, G. 2018, MNRAS, 473, 5050

Bauer, J. M., Mainzer, A. K., Grav, T., et al. 2012, ApJ, 747, 49

Bellm, E. C., Kulkarni, S. R., Graham, M. J., et al. 2019, PASP, 131, 018002

Berthier, J., Carry, B., Mahlke, M., & Normand, J. 2023, A&A, 671, A151

Berthier, J., Hestroffer, D., Carry, B., et al. 2008, LPI Contributions, 1405, 8374

Birlan, M., Barucci, M. A., Angeli, C. A., Doressoundiram, A., & De Sanctis, M. C. 1996, Planet. Space Sci., 44, 555

Borucki, W. J., Koch, D., Basri, G., et al. 2010, Science, 327, 977

Bottke, W. F., Vokrouhlický, D., Broz, M., Nesvorný, D., & Morbidelli, A. 2001, Science, 294, 1693

Bottke, W. F., Vokrouhlický, D., Walsh, K. J., et al. 2015, Icarus, 247, 191

Bowell, E., Hapke, B., Domingue, D., et al. 1989, Asteroids II, 524

Brownlee, D., Tsou, P., Aléon, J., et al. 2006, Science, 314, 1711

Carry, B. 2012, Planet. Space Sci., 73, 98

Carry, B. 2018, A&A, 609, A113

Carry, B., Peloton, J., Le Montagner, R., Mahlke, M., & Berthier, J. 2024, A&A, 687, A38

Carvano, J. M., Hasselmann, P. H., Lazzaro, D., & Mothé-Diniz, T. 2010, A&A, 510, A43

Cellino, A., Hestroffer, D., Lu, X. P., Muinonen, K., & Tanga, P. 2019, A&A, 631, A67

Cellino, A., Tanga, P., Muinonen, K., & Mignard, F. 2024, A&A, 687, A277

Chang, C.-K., Ip, W.-H., Lin, H.-W., et al. 2015, ApJS, 219, 27

Clement, M. S., Morbidelli, A., Raymond, S. N., & Kaib, N. A. 2020, MNRAS, 492, L56

Cloutis, E. A., Sanchez, J. A., Reddy, V., et al. 2015, Icarus, 252, 39

Colazo, M., Oszkiewicz, D., Alvarez-Candal, A., et al. 2025, Icarus, 436, 116577

Connelly, R. & Ostro, S. J. 1984, Geometriae Dedicata (ISSN 0046-5755, 17, 87

[9] http://www.astropy.org
[10] https://sbpy.org/
[11] https://github.com/maxmahlke/rocks

Conversi, L., Licandro, J., Delbo, M., et al. 2024, in Society of Photo-Optical Instrumentation Engineers (SPIE) Conference Series, Vol. 13092, Space Telescopes and Instrumentation 2024: Optical, Infrared, and Millimeter Wave, ed. L. E. Coyle, S. Matsuura, & M. D. Perrin, 130922H
Debehogne, H. & Zappala, V. 1980, A&AS, 40, 257
DeMeo, F. E., Burt, B. J., Marsset, M., et al. 2022, Icarus, 380, 114971
DeMeo, F. E. & Carry, B. 2013, Icarus, 226, 723
DeMeo, F. E. & Carry, B. 2014, Nature, 505, 629
Ďurech, J., Carry, B., Delbo, M., Kaasalainen, M., & Viikinkoski, M. 2015, Asteroid Models from Multiple Data Sources (Univ. Arizona Press), 183–202
Farinella, P., Vokrouhlický, D., & Hartmann, W. K. 1998, Icarus, 132, 378
French, L. M. 1987, Icarus, 72, 325
Galluccio, L., Delbo, M., De Angeli, F., et al. 2023, A&A, 674, A35
Garrison, L. H., Foreman-Mackey, D., hsuan Shih, Y., & Barnett, A. 2024, Research Notes of the AAS, 8, 250
Goutte, C. & Gaussier, E. 2005, in Advances in Information Retrieval, ed. D. E. Losada & J. M. Fernández-Luna (Berlin, Heidelberg: Springer Berlin Heidelberg), 345–359
Gradie, J. & Tedesco, E. F. 1982, Science, 216, 1405
Grav, T., Mainzer, A. K., Bauer, J., et al. 2011, ApJ, 742, 40
Hanuš, J., Ďurech, J., Oszkiewicz, D. A., et al. 2016, A&A, 586, A108
Hasegawa, S., Müller, T. G., Kuroda, D., Takita, S., & Usui, F. 2013, PASJ, 65, 34
Hirayama, K. 1918, AJ, 31, 185
Howell, S. B., Sobeck, C., Haas, M., et al. 2014, PASP, 126, 398
IMCCE. 2021, Introduction aux éphémérides et phénomènes astronomiques, ed. J. Berthier, P. Descamps, & F. Mignard (edp sciences)
Ivezić, Ž., Kahn, S. M., Tyson, J. A., et al. 2019, ApJ, 873, 111
Jackson, S. L., Rozitis, B., Dover, L. R., et al. 2022, MNRAS, 513, 3076
Jiang, H. & Ji, J. 2021, AJ, 162, 40
Johansen, A., Mac Low, M.-M., Lacerda, P., & Bizzarro, M. 2015, Science Advances, 1, 1500109
Kaasalainen, M. 2001, A&A, 376, 302
Kaasalainen, M. 2004, A&A, 422, L39
Kaasalainen, M. & Torppa, J. 2001, Icarus, 153, 24
Kaasalainen, M., Torppa, J., & Muinonen, K. 2001, Icarus, 153, 37
Kecskeméthy, V., Kiss, C., Szakáts, R., et al. 2023, ApJS, 264, 18
Kurlander, J. A., Bernardinelli, P. H., Schwamb, M. E., et al. 2025, AJ, 170, 99
Lagerros, J. S. V. 1996, A&A, 310, 1011
Lauretta, D. S., Connolly, H. C., Aebersold, J. E., et al. 2024, Meteoritics and Planetary Science, 59, 2453
Law, N. M., Kulkarni, S. R., Dekany, R. G., et al. 2009, PASP, 121, 1395
Lomb, N. R. 1976, Ap&SS, 39, 447
LSST Science Collaboration, Abell, P. A., Allison, J., et al. 2009, arXiv e-prints, arXiv:0912.0201
Lu, X., Zhao, H., & You, Z. 2014, Earth Moon and Planets, 112, 73
Mahlke, M., Carry, B., & Denneau, L. 2021, Icarus, 354, 114094
Mahlke, M., Carry, B., & Mattei, P. A. 2022, A&A, 665, A26
Mahlke, M., Marsset, M., Devogèle, M., et al. 2026, A&A, 705, A121
Mainzer, A., Grav, T., Bauer, J., et al. 2011, ApJ, 743, 156
Mainzer, A. K., Masiero, J. R., Abell, P. A., et al. 2023, Planetary Science Journal, 4, 224
Marchis, F., Lainey, V., Descamps, P., et al. 2010, Icarus, 210, 635
Marciniak, A., Bartczak, P., Müller, T., et al. 2018, A&A, 610, A7
Masci, F. J., Laher, R. R., Rusholme, B., et al. 2019, PASP, 131, 018003
Masiero, J. R., Mainzer, A. K., Grav, T., et al. 2011, ApJ, 741, 68
McCheyne, R. S., Eaton, N., & Meadows, A. J. 1985, Icarus, 61, 443
McCord, T. B., Adams, J. B., & Johnson, T. V. 1970, Science, 168, 1445
McMahon, R. G., Banerji, M., Gonzalez, E., et al. 2013, The Messenger, 154, 35
Merritt, S., Fedorets, G., Schwamb, M., et al. 2025, The Journal of Open Source Software, 10, 8145
Möller, A., Peloton, J., Ishida, E. E. O., et al. 2021, MNRAS, 501, 3272
Mommert, M., Kelley, M., de Val-Borro, M., et al. 2019, The Journal of Open Source Software, 4, 1426
Morbidelli, A., Baillié, K., Batygin, K., et al. 2022, Nature Astronomy, 6, 72
Morrison, D. 1974, ApJ, 194, 203
Moskovitz, N. A., Lawrence, S., Jedicke, R., et al. 2008, ApJ, 682, L57
Muinonen, K., Belskaya, I. N., Cellino, A., et al. 2010, Icarus, 209, 542
Muinonen, K., Torppa, J., Wang, X. B., Cellino, A., & Penttilä, A. 2020, A&A, 642, A138
Murakami, H., Baba, H., Barthel, P., et al. 2007, PASJ, 59, S369
Nakamura, T., Matsumoto, M., Amano, K., et al. 2023, Science, 379, abn8671
Nakamura, T., Noguchi, T., Tanaka, M., et al. 2011, Science, 333, 1113
Neugebauer, G., Habing, H. J., van Duinen, R., et al. 1984, ApJ, 278, L1
Neveu, M. & Vernazza, P. 2019, ApJ, 875, 30
Novaković, B., Vokrouhlický, D., Spoto, F., & Nesvorný, D. 2022, Celestial Mechanics and Dynamical Astronomy, 134, 34
Ostro, S. J. & Connelly, R. 1984, Icarus, 57, 443
Oszkiewicz, D., Bartczak, P., Colazo, M., & Penttilä, A. 2026, Icarus, 446, 116886
Pál, A., Szakáts, R., Kiss, C., et al. 2020, ApJS, 247, 26
Pilcher, F. 2012, Minor Planet Bulletin, 39, 171
Popescu, M., Licandro, J., Carvano, J. M., et al. 2018, A&A, 617, A12
Popescu, M., Licandro, J., Morate, D., et al. 2016, A&A, 591, A115
Press, W. H. & Rybicki, G. B. 1989, ApJ, 338, 277
Prusti, T., de Bruijne, J. H. J., Brown, A. G. A., et al. 2016, A&A, 595, A1
Ricker, G. R., Winn, J. N., Vanderspek, R., et al. 2015, Journal of Astronomical Telescopes, Instruments, and Systems, 1, 014003
Rodrigo, C. & Solano, E. 2020, in XIV.0 Scientific Meeting (virtual) of the Spanish Astronomical Society, 182
Rodrigo, C., Solano, E., & Bayo, A. 2012, SVO Filter Profile Service Version 1.0, IVOA Working Draft 15 October 2012
Roodman, A., Rasmussen, A., Bradshaw, A., et al. 2024, in Society of Photo-Optical Instrumentation Engineers (SPIE) Conference Series, Vol. 13096, Ground-based and Airborne Instrumentation for Astronomy X, ed. J. J. Bryant, K. Motohara, & J. R. D. Vernet, 130961S
Russell, H. N. 1906, ApJ, 24, 1
Sanchez, J. A., Reddy, V., Nathues, A., et al. 2012, Icarus, 220, 36
Scargle, J. D. 1982, ApJ, 263, 835
Scheeres, D. J., Britt, D., Carry, B., & Holsapple, K. A. 2015, Asteroid Interiors and Morphology, ed. P. Michel, F. DeMeo, & W. F. Bottke (Univ. Arizona Press), 745–766
Scheirich, P. & Pravec, P. 2009, Icarus, 200, 531
Schober, H. J. & Dvorak, R. 1975, A&A, 44, 81
Schwarzenberg-Czerny, A. 1996, ApJ, 460, L107
Scott, E. R. D., Krot, A. N., & Sanders, I. S. 2018, ApJ, 854, 164
Sergeyev, A. V. & Carry, B. 2021, A&A, 652, A59
Sergeyev, A. V., Carry, B., Onken, C. A., et al. 2022, A&A, 658, A109
Statler, T. S. 2009, Icarus, 202, 502
Stellingwerf, R. F. 1978, ApJ, 224, 953
Surdej, A. & Surdej, J. 1977, A&AS, 30, 121
Sykes, M. V., Cutri, R. M., Fowler, J. W., et al. 2000, Icarus, 146, 161
Tanga, P., Pauwels, T., Mignard, F., et al. 2023, A&A, 674, A12
Taylor, M. B. 2005, in Astronomical Society of the Pacific Conference Series, Vol. 347, Astronomical Data Analysis Software and Systems XIV, ed. P. Shopbell, M. Britton, & R. Ebert, 29
Thirouin, A., Moskovitz, N. A., Binzel, R. P., et al. 2018, ApJS, 239, 4
Tholen, D. J. 1984, PhD thesis, Arizona Univ., Tucson.
Tonry, J. L., Denneau, L., Heinze, A. N., et al. 2018, PASP, 130, 064505
Usui, F., Kuroda, D., Müller, T. G., et al. 2011, PASJ, 63, 1117
VanderPlas, J. T. 2018, ApJS, 236, 16
VanderPlas, J. T. & Ivezić, Ž. 2015, ApJ, 812, 18
Vavilov, D. E. & Carry, B. 2025, A&A, 693, A66
Ďurech, J. & Hanuš, J. 2023, A&A, 675, A24
Ďurech, J., Hanuš, J., & Alí-Lagoa, V. 2018, A&A, 617, A57
Ďurech, J., Hanuš, J., Oszkiewicz, D., & Vančo, R. 2016, A&A, 587, A48
Ďurech, J., Hanuš, J., & Vančo, R. 2015, Astronomy and Computing, 13, 80
Ďurech, J., Tonry, J., Erasmus, N., et al. 2020, A&A, 643, A59
Ďurech, J., Vávra, M., Vančo, R., & Erasmus, N. 2022, Frontiers in Astronomy and Space Sciences, 9, 809771
Vernazza, P., Ferrais, M., Jorda, L., et al. 2021, A&A, 654, A56
Vokrouhlický, D., Bottke, W. F., Chesley, S. R., Scheeres, D. J., & Statler, T. S. 2015, The Yarkovsky and YORP Effects, ed. P. Michel, F. DeMeo, & W. F. Bottke, 509–531
Walsh, K. J., Morbidelli, A., Raymond, S. N., O'Brien, D. P., & Mandell, A. M. 2011, Nature, 475, 206
Wasserman, L. H., Millis, R. L., Franz, O. G., et al. 1979, AJ, 84, 259
Waszczak, A., Chang, C.-K., Ofek, E. O., et al. 2015, AJ, 150, 75
Wolf, C., Onken, C. A., Luvaul, L. C., et al. 2018, PASA, 35, e010
Wright, E. L., Eisenhardt, P. R. M., Mainzer, A. K., et al. 2010, AJ, 140, 1868
Zhou, W.-H. & Michel, P. 2024, A&A, 682, A130
Zhou, W.-H., Michel, P., Delbo, M., et al. 2025, Nature Astronomy, 9, 493

Appendix A: Spheroid and ellipsoid models

We detail here the computation of the shape-related $s(\alpha,\delta,t)$ function used in SOCCA. First, we recall the $s(\alpha,\delta)$ from $\mathtt{sHG_1G_2}$ (Carry et al. 2024):

$$\begin{aligned} s(\alpha,\delta,t) &= s(\alpha,\delta) \\ &= 2.5\log_{10}\left[1-(1-R)|\cos\Lambda|\right], \end{aligned} \tag{A.1}$$

where $0 < R \leq 1$ is the oblateness of the spheroid

$$R = \frac{c(a+b)}{2ab}, \tag{A.2}$$

and the aspect angle Λ is computed from the coordinates (α_0,δ_0) of the spin axis and the coordinates (α,δ) of the asteroid as seen from the observer (IMCCE 2021):

$$\cos\Lambda = \sin\delta\sin\delta_0 + \cos\delta\cos\delta_0\cos(\alpha-\alpha_0), \tag{A.3}$$

The new $s(\alpha,\delta,t)$ of SOCCA is computed from the projection of an ellipsoid on the plane of the sky:

$$s(\alpha,\delta,t) = 2.5\log_{10}\mathcal{A}. \tag{A.4}$$

To compute it, we define $(\varphi, 90-\Lambda)$ and $(\varphi_s, 90-\Lambda_s)$ the planetocentric coordinates of the sub-observer and subsolar point on the target. The unit vectors $\boldsymbol{e}$ and $\boldsymbol{s}$ to the observer and to the Sun are thus

$$\boldsymbol{e} = \begin{pmatrix} e_1 \\ e_2 \\ e_3 \end{pmatrix} = \begin{pmatrix} \sin\Lambda\cos\varphi \\ \sin\Lambda\sin\varphi \\ \cos\Lambda \end{pmatrix} \tag{A.5}$$

$$\boldsymbol{s} = \begin{pmatrix} s_1 \\ s_2 \\ s_3 \end{pmatrix} = \begin{pmatrix} \sin\Lambda_s\cos\varphi_s \\ \sin\Lambda_s\sin\varphi_s \\ \cos\Lambda_s \end{pmatrix}. \tag{A.6}$$

We then follow the formalism by Ostro & Connelly (1984) to compute the projected surface area $\mathcal{A}$ of an ellipsoid at opposition (phase angle $\gamma = 0^{\mathrm{o}}$) by introducing the matrix $\boldsymbol{Q}$ as

$$\boldsymbol{Q} = \begin{pmatrix} 1/a^2 & 0 & 0 \\ 0 & 1/b^2 & 0 \\ 0 & 0 & 1/c^2 \end{pmatrix} \tag{A.7}$$

$$\mathcal{A} = S_1 = \pi abc\left(\boldsymbol{e}^t\boldsymbol{Q}\boldsymbol{e}\right)^{1/2}, \tag{A.8}$$

where ^{t} indicates transposition, $a \geq b \geq c$ are the semimajor axes of the ellipsoid, and with

$$\boldsymbol{e}^t\boldsymbol{Q}\boldsymbol{e} = \frac{\sin^2\Lambda\cos^2\varphi}{a^2} + \frac{\sin^2\Lambda\sin^2\varphi}{b^2} + \frac{\cos^2\Lambda}{c^2}. \tag{A.9}$$

The generalisation to non-zero phase angle ($\gamma > 0^{\mathrm{o}}$) is based on a partially illuminated ellipsoid (Connelly & Ostro 1984), which apparent surface is delimited by the limb on one side and the terminator on the other, hence

$$\mathcal{A} = \frac{S_1+S_2}{2}, \tag{A.10}$$

where

$$S_2 = \pi abc\left[\frac{\boldsymbol{e}^t\boldsymbol{Q}\boldsymbol{s}}{\left(\boldsymbol{s}^t\boldsymbol{Q}\boldsymbol{s}\right)^{1/2}}\right], \tag{A.11}$$

in which $\boldsymbol{s}^t\boldsymbol{Q}\boldsymbol{s}$ is computed with Eq. A.9 by replacing (φ,Λ) by (φ_s,Λ_s), and

$$\begin{aligned} \boldsymbol{e}^t\boldsymbol{Q}\boldsymbol{s} &= \frac{\sin\Lambda\cos\varphi\sin\Lambda_s\cos\varphi_s}{a^2} \\ &+ \frac{\sin\Lambda\sin\varphi\sin\Lambda_s\sin\varphi_s}{b^2} \\ &+ \frac{\cos\Lambda\cos\Lambda_s}{c^2}. \end{aligned} \tag{A.12}$$

S_2 area is signed, to account for cases in which the phase angle is above 90$^{\mathrm{o}}$, i.e., the apparent surface is a lunula and not an ellipsoid. The $s(\alpha,\delta,t)$ differs from the total flux from the projected surface $-2.5\log_{10}\mathcal{A}$ by a constant offset $-2.5\log_{10}\pi bc$, i.e., the magnitude of the minimum projected surface. This offset is incorporated in the absolute magnitude H, which then is defined as the magnitude of the object at 1 au from both the Sun and the observer, with a 0$^{\mathrm{o}}$ phase angle, seen from its equatorial plane and its prime meridian.

Following the IAU recommendation (Archinal et al. 2018) and the recipes in IMCCE (2021), the sub-observer longitude (rotation phase φ) is computed as follows:

$$\tan(W-\varphi) = \frac{\cos\delta_0\sin\delta - \sin\delta_0\cos\delta\cos(\alpha-\alpha_0)}{\cos\delta\sin(\alpha-\alpha_0)}, \tag{A.13}$$

with W the longitude of the prime meridian at the time of observation, computed as

$$W = W_0 + \dot{W}(t-t_0), \text{ with} \tag{A.14}$$

$$\dot{W} = \frac{2\pi}{\mathtt{P_{sid}}} \tag{A.15}$$

from an initial angle W_0 at a reference epoch t_0. The IAU recommendation is to take t_0 as J2000 (Archinal et al. 2018). It is, however, a transparent parameter and can be arbitrarily chosen at any epoch. As the uncertainty on the prime meridian longitude W grows linearly with time (Appendix A), leading to an uncertain orientation of the shape, it is more accurate to tie t_0 with the epochs of observations. We typically taken the mid-epoch of observations to minimize the de-phasing issue linked with the reference epoch t_0.

Appendix B: Model re-parametrization

For practical numerical purposes such as the stability of the inversion and the efficiency of the convergence, most parameters are remapped into latent variables. This allows each physical parameter to remain within a valid range while the optimized parameters are defined on $\mathbb{R}$. We mainly use the following sigmoid function $\mathtt{sig}(x)$, defined on $\mathbb{R}$ and bounded to $]R, R+|C|[$, and its inverse function logit(x) to convert variables to or from latent variables:

$$\mathtt{sig}(x) = C + \frac{R}{1+e^{-x}} \tag{B.1}$$

$$\mathrm{logit}(p) = \log\frac{p}{1-p}, \quad p = \frac{x-C}{R}. \tag{B.2}$$

The absolute magnitude H and the sidereal rotation period $\mathtt{P_{sid}}$ being already defined on $\mathbb{R}$, we leave them untouched. The axes ratios a/b and a/c are computed from the latent variables $u_{a/b}$ and $u_{a/c}$ using

$$\begin{aligned} \mathtt{a/b} &= 4\,\mathtt{sig}(u_{a/b}) + 1 & \text{(B.3)}\\ \mathtt{a/c} &= (5 - \mathtt{a/b})\,\mathtt{sig}(u_{a/c}) + \mathtt{a/b}, & \text{(B.4)}\\ && \text{(B.5)} \end{aligned}$$

with $R = 1$ and $C = 0$. This ensures that $1 < \mathtt{a/b} < \mathtt{a/c} < 5$. The upper limit is somewhat arbitrary but chosen to encompass extreme shapes. The condition between a/b and a/c is required for principal axis rotator such as described by SOCCA. Similarly to the axes ratio, we re-map the $\mathtt{G}_1\mathtt{G}_2$ phase function parameters into the latent variables $u_{\mathtt{G}_1}$ and $u_{\mathtt{G}_2}$:

$$\begin{aligned} \mathtt{G}_1 &= \mathtt{sig}_1(u_{\mathtt{G}_1}) & \text{(B.6)}\\ \mathtt{G}_2 &= L + (U - L)\,\mathtt{sig}_2(u_{\mathtt{G}_2}), & \text{(B.7)} \end{aligned}$$

with $\mathtt{sig}_1$ computed with $R = G_{\max} + |G_{\min}|$ and $C = G_{\min}$ and L, U given by

$$\begin{aligned} L &= \max\left(G_{\min},\ a_1\mathtt{G}_1 + b_1,\ a_3\mathtt{G}_1\right) & \text{(B.8)}\\ U &= \min\left(G_{\max},\ a_2\mathtt{G}_1 + b_2\right), & \text{(B.9)} \end{aligned}$$

where

$$\begin{aligned} G_{\min} &= -0.429 \qquad G_{\max} = 1.429 & \text{(B.10)}\\ a_1 &= -3.9038 \qquad b_1 = -0.2445 & \text{(B.11)}\\ a_2 &= -0.9635 \qquad b_2 = 1.0157 & \text{(B.12)}\\ a_3 &= -0.4 & \text{(B.13)} \end{aligned}$$

from the constraints given by Eqs. 4a-4c. The initial rotation phase W_0, bounded to $[-\pi/2, \pi/2]$, is recovered from its latent representation u_{W_0} as

$$W_0 = \pi\,\mathtt{sig}(u_{W_0}) - \frac{\pi}{2}, \tag{B.14}$$

with $R = 1$ and $C = 0$

Finally, to account for the spherical geometry, the spin axis coordinates α_0 and δ_0 are expressed in latent Cartesian coordinates (X, Y, Z), and expressed as

$$\begin{aligned} \rho &= \sqrt{X^2 + Y^2 + Z^2} & \text{(B.15)}\\ \delta_0 &= \arcsin\frac{Z}{\rho} & \text{(B.16)}\\ \alpha_0 &= \arctan\frac{Y}{X}. & \text{(B.17)} \end{aligned}$$

Appendix C: Error calculation

The uncertainty on each fitted latent parameter is estimated from the covariance matrix derived from the Jacobian of the optimal least squares solution. Let $\mathbf{r}$ be the vector of residuals and $\mathbf{J}$ the Jacobian matrix of partial derivatives evaluated at the solution $\mathbf{u}$ in latent space. The covariance matrix of the parameters is approximated by

$$\mathbf{C} = \left(\mathbf{J}^{\mathsf{T}}\mathbf{J}\right)^{-1}\chi^2_\nu \tag{C.1}$$

where χ^2_ν is the reduced chi-square of the fit,

$$\chi^2_\nu = \frac{\sum_i r_i^2}{N - M} \tag{C.2}$$

with N the number of observations and M the number of fitted parameters. The 1σ uncertainty on each latent parameter u_i is then obtained from the diagonal elements of the covariance matrix,

$$\sigma_{u_i} = \sqrt{C_{ii}} \tag{C.3}$$

Since the model parameters are optimized in latent space, the uncertainties on the corresponding physical parameters are obtained through standard error propagation. For a physical parameter $p = f(\mathbf{u_i})$ expressed as a function of N latent variables $\mathbf{u_i}$, the variance is

$$\sigma_p^2 = \left(\sum_{k=1}^{N}\frac{\partial f}{\partial u_i}\sigma_{u_i}\right)^2 \tag{C.4}$$

Using the transformations defined in Eq. B.3, the propagated 1σ uncertainties on the physical shape parameters a/b and a/c are

$$\sigma_{\mathtt{a/b}} = 4\,\mathtt{sig}(u_{\mathtt{a/b}})\left[1 - \mathtt{sig}(u_{\mathtt{a/b}})\right]\,\sigma_{u_{\mathtt{a/b}}} \tag{C.5}$$

$$\begin{aligned} \sigma_{\mathtt{a/c}} = \Big(&\left[(1 - \mathtt{sig}(u_{\mathtt{a/c}}))\,\sigma_{\mathtt{a/b}}\right]^2\\ &+ \left[(5 - \mathtt{a/b})\,\mathtt{sig}(u_{\mathtt{a/c}})(1 - \mathtt{sig}(u_{\mathtt{a/c}}))\,\sigma_{u_{\mathtt{a/c}}}\right]^2\\ &+ 2(1 - \mathtt{sig}(u_{\mathtt{a/c}}))(5 - \mathtt{a/b})\,\mathtt{sig}(u_{\mathtt{a/c}})\\ &\times (1 - \mathtt{sig}(u_{\mathtt{a/c}}))\,\sigma_{u_{\mathtt{a/c}}}\sigma_{\mathtt{a/b}}\Big)^{1/2}, \end{aligned} \tag{C.6}$$

with $R = 1$ and $C = 0$. Similarly, we propagate the uncertainties for $\mathtt{G}_1$ and $\mathtt{G}_2$ from Eqs. B.6 and B.7 as follows:

$$\begin{aligned} \sigma_{\mathtt{G}_1} &= R\frac{e^{-u_{\mathtt{G}_1}}}{(e^{-u_{\mathtt{G}_1}} + 1)^2}\sigma_{u_{\mathtt{G}_1}} & \text{(C.7)}\\ \sigma_{\mathtt{G}_2} &= (U - L)(1 - \mathtt{sig}(u_{\mathtt{G}_2}))\mathtt{sig}(u_{\mathtt{G}_2})\sigma_{u_{\mathtt{G}_2}}, & \text{(C.8)} \end{aligned}$$

with R, L and U computed similarly as in Eqs. B.6 and B.7. The uncertainty of the initial phase W_0 from Eq. B.14 is

$$\sigma_{W_0} = \pi\mathtt{sig}(u_{W_0})(1 - \mathtt{sig}(u_{W_0}))\sigma_{u_{W_0}}, \tag{C.9}$$

with $R = 1$ and $C = 0$. The uncertainty of the spin axis coordinates α_0 and δ_0 is retrieved form the directional covariance of their latent counterparts given in Eqs. B.15–B.17. As α_0 and δ_0 describe the direction of the spin vector, the magnitude ρ has no physical meaning and is not constrained by the photometric data. It is only used as it is necessary for the chosen re-parametrization. Nonetheless it introduces some non-physical variance which should not be accounted for. Therefore, we compute the directional covariance of the X, Y, and Z parameters as follows:

$$\begin{aligned} \mathbf{v} &= (X, Y, Z) & \text{(C.10)}\\ \mathbf{n} &= \frac{\mathbf{v}}{\|\mathbf{v}\|} & \text{(C.11)}\\ \mathbf{P} &= \mathbf{I} - \mathbf{n}\mathbf{n}^T & \text{(C.12)}\\ \mathbf{C}_{\mathrm{dir}} &= \mathbf{P}\,\mathbf{C}_{XYZ}\,\mathbf{P}, & \text{(C.13)} \end{aligned}$$

where $\mathbf{I}$ is the identity matrix. The uncertainties of the latent parameters are given by the square of the diagonal element of the 3×3 matrix $\mathbf{C}_{\mathrm{dir}}$.

From these uncertainties we can retrieve the uncertainties of α_0 and δ_0 as follows:

$$\frac{\partial \delta_0}{\partial X} = -\frac{XZ}{\sqrt{1-\frac{Z^2}{X^2+Y^2+Z^2}}\,(X^2+Y^2+Z^2)^{3/2}} \tag{C.14}$$

$$\frac{\partial \delta_0}{\partial Y} = -\frac{YZ}{\sqrt{1-\frac{Z^2}{X^2+Y^2+Z^2}}\,(X^2+Y^2+Z^2)^{3/2}} \tag{C.15}$$

$$\begin{aligned} \frac{\partial \delta_0}{\partial Z} &= \left(\frac{1}{\sqrt{X^2+Y^2+Z^2}} - \frac{Z^2}{(X^2+Y^2+Z^2)^{3/2}}\right) \\ &\times \frac{1}{\sqrt{1-\frac{Z^2}{X^2+Y^2+Z^2}}} \end{aligned} \tag{C.16}$$

$$\begin{aligned} \sigma_{\delta_0} &= \sqrt{\left(\frac{\partial \delta_0}{\partial X}\sigma_X\right)^2 + \left(\frac{\partial \delta_0}{\partial Y}\sigma_Y\right)^2 + \left(\frac{\partial \delta_0}{\partial Z}\sigma_Z\right)^2} \\ &\quad + 2\left(\frac{\partial \delta_0}{\partial X}\frac{\partial \delta_0}{\partial Y}\sigma_X\sigma_Y + \frac{\partial \delta_0}{\partial X}\frac{\partial \delta_0}{\partial Z}\sigma_X\sigma_Z\right. \\ &\quad \left. + \frac{\partial \delta_0}{\partial Y}\frac{\partial \delta_0}{\partial Z}\sigma_Y\sigma_Z\right) \end{aligned} \tag{C.17}$$

$$\begin{aligned} \sigma_{\alpha_0} &= \left(\left(\left(\frac{X}{X^2+Y^2}\sigma_Y\right)^2 + \left(\frac{Y}{X^2+Y^2}\sigma_X\right)^2\right)\right. \\ &- \left.\frac{XY}{(X^2+Y^2)^2}\sigma_X\sigma_Y\right)^{1/2}. \end{aligned} \tag{C.18}$$

Appendix D: $\mathtt{G}_1$ and $\mathtt{G}_2$ distributions per model

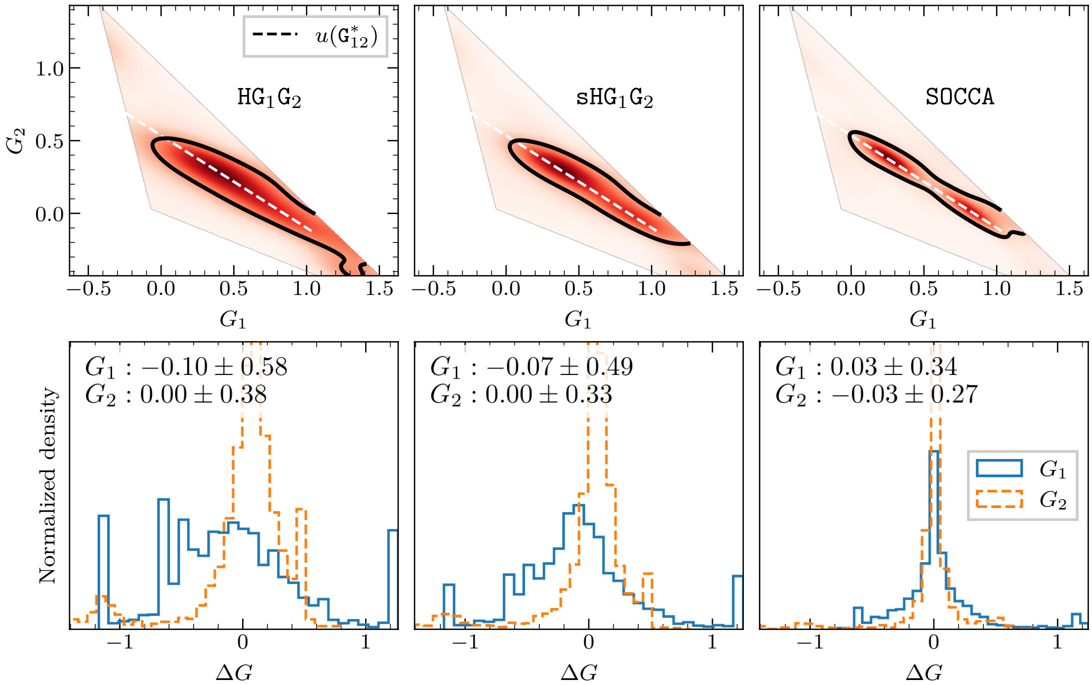

Fig. D.1: Distribution of $\mathtt{G_1G_2}$ parameters for the different models. *Top*: Gaussian kernel density estimators (KDEs) of $\mathtt{G_1G_2}$ for the $\mathtt{HG_1G_2}$, $\mathtt{sHG_1G_2}$, and SOCCA model. The contour encloses 68% of the integrated probability, corresponding to the 1σ level of a Gaussian distribution. The white dash line represents the $\mathtt{G}^*_{12}$ phase parameter of the phase curves. *Bottom*: Distribution of the difference between the simulated and retrieved $\mathtt{G_1}$ and $\mathtt{G_2}$ for each model.